INVESTIGATION OF THE PASCHEN CURVE OF NITROGEN VIA THE APPLICATION OF NANOSECOND PULSED ELECTROMAGNETIC RADIATION
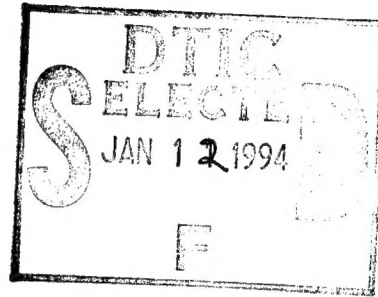
David W. Scholfield

DTIC
ELECTE
JAN 12 1994
F

December 1994

Final Report

19950109 059

PHILLIPS LABORATORY
Advanced Weapons and Survivability Directorate
AIR FORCE MATERIEL COMMAND
KIRTLAND AIR FORCE BASE, NM 87117-5776

PL-TR--94-1125

This final report was prepared by the Phillips Laboratory, Kirtland Air Force Base, New Mexico, under Job Order 3152AN02. Dr David W. Scholfield (WSR) was the Laboratory Project Officer-in-Charge.
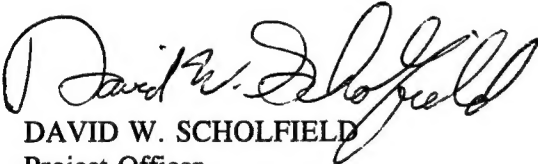
This technical report has been reviewed and is approved for publication.

DAVID W. SCHOLFIELD
Project Officer

FOR THE COMMANDER

FORREST J. AGEE, GM-15
Chief, Electromagnetic Sources
Division

WILLIAM L. BAKER, GM-15
Acting Director, Advanced Weapons and
Survivability Directorate

DO NOT RETURN COPIES OF THIS REPORT UNLESS CONTRACTUAL OBLIGATIONS OR NOTICE
ON A SPECIFIC DOCUMENT REQUIRES THAT IT BE RETURNED.

1. AGENCY USE ONLY *(Leave blank)*	2. REPORT DATE December 1994	3. REPORT TYPE AND DATES COVERED Final 1 Aug 90 - 1 Aug 93

4. TITLE AND SUBTITLE
INVESTIGATION OF THE PASCHEN CURVE OF NITROGEN VIA THE APPLICATION OF NANOSECOND PULSED ELECTROMAGNETIC RADIATION

5. FUNDING NUMBERS
PE: 63605F
PR: 3152
TA: AN
WU: 02

6. AUTHOR(S)
David W. Scholfield

7. PERFORMING ORGANIZATION NAME(S) AND ADDRESS(ES)
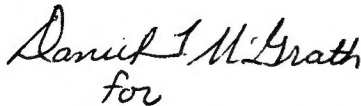
Phillips Laboratory
3550 Aberdeen Ave SE
Kirtland AFB, NM 87117-5776

8. PERFORMING ORGANIZATION REPORT NUMBER

PL-TR--94-1125

9. SPONSORING / MONITORING AGENCY NAME(S) AND ADDRESS(ES)

10. SPONSORING / MONITORING AGENCY REPORT NUMBER

11. SUPPLEMENTARY NOTES
Publication of this technical report does not constitute approval or disapproval of the ideas or findings. It is published in the interest of STINFO exchange. The established procedures for editing reports were not followed for this report.

12a. DISTRIBUTION / AVAILABILITY STATEMENT

Approved for public release; distribution is unlimited.

12b. DISTRIBUTION CODE

13. ABSTRACT *(Maximum 200 words)*

In order to obtain lasing in microwave excited gases, a knowledge of the Paschen curve is required so that estimates can be made of the required intensity of the electromagnetic field for a given pulse duration. Data in the region below 10^{-8} Torr-s with electromagnetic fields in excess of 10 kV/cm/Torr had been unobtainable due to technical limitations. The Paschen curve of nitrogen from pressures of 0.336 Torr to 685 Torr via the application of nanosecond pulsed electromagnetic radiation has been investigated. Breakdown of the gas was achieved through pumping by short electromagnetic pulses and verified through the use of an optical multichannel analyzer. Previous investigations have utilized monofrequency electromagnetic signals. Adjustments for the short pulse nature of this investigation have been derived and are applied to the Paschen curve. Experiments have been conducted utilizing a pulser with machine parameters of 1 J delivered during 1.375 ns FWHM into a 50 Ω coaxial line, at a peak power of 1 GW. By investigating this previously unexplored region, data have been acquired in the region of the relativistic Paschen curve as hypothesized by Graham and Roussel-Dupre. Experimental results yield no observable relativistic effects under the conditions of this experiment. Additionally, the collisional frequency limit has been experimentally identified.

14. SUBJECT TERMS
Paschen Curve, Gaseous Breakdown, Short Electromagnetic Pulse

15. NUMBER OF PAGES
122

16. PRICE CODE

17. SECURITY CLASSIFICATION OF REPORT Unclassified	18. SECURITY CLASSIFICATION OF THIS PAGE Unclassified	19. SECURITY CLASSIFICATION OF ABSTRACT Unclassified	20. LIMITATION OF ABSTRACT

DEDICATION

To my devoted wife, Diane, and my sons: Gregory, Matthew, and
Daniel.   They stood by me and were a wife and family to me,
when studies and dissertation work would not allow me to be
either a husband or father to them.

iii

Mr. William Green for providing the acquisition support for my project.

Dr. Thomas Spencer for changing his password on his PC so that I couldn't waste my time playing Strategic Conquest.

Mr. Charles Davis and Ms. Melissa Douglas for all the french fries and delightful conversations.

Capt. Alex Pilipowskyj, who wished to be recognized in this document.

Moose...

ACKNOWLEDGEMENTS

INVESTIGATION OF

THE PASCHEN CURVE OF NITROGEN

VIA THE APPLICATION OF NANOSECOND

PULSED ELECTROMAGNETIC RADIATION

BY

DAVID W. SCHOLFIELD

ABSTRACT OF DISSERTATION

Submitted in Partial Fulfillment of the

Requirements for the Degree of

Doctor of Philosophy in Electrical Engineering

The University of New Mexico

Phillips Laboratory/WSR

Albuquerque, New Mexico

July 1993

ABSTRACT

INVESTIGATION OF
THE PASCHEN CURVE OF NITROGEN
VIA THE APPLICATION OF NANOSECOND
PULSED ELECTROMAGNETIC RADIATION

David W. Scholfield

B.S., Wichita State University, Wichita KS., 1980

M.S., University of New Mexico, 1990

In order to obtain lasing in microwave excited gases a knowledge of the Paschen curve is required so that estimates can be made of the required intensity of the electromagnetic field for a given pulse duration. Data in the region below 10^{-8} Torr-s with electromagnetic fields in excess of 10kV/cm/Torr had been unobtainable due to technical limitations. If accurate lasing research via microwave pumping is to be done in this region, experimental data must be obtained to either validate or repudiate current theory relating to this region. An investigation of the Paschen curve of nitrogen from pressures of 0.336 Torr to 685 Torr via the application of nanosecond pulsed electromagnetic radiation has been investigated. Breakdown of the gas was achieved via pumping by short electromagnetic pulses and verified through

the use of an optical multichannel analyzer. Previous investigations have utilized monofrequency electromagnetic signals. Adjustments for the short pulse nature of this investigation have been derived and are applied to the Paschen curve. Experiments have been conducted utilizing a pulser with machine parameters of 1 J delivered during 1.375 ns FWHM into a 50 Ω coaxial line, at a peak power of 1 GW. By investigating this previously unexplored region, data has been acquired in the region of the relativistic Paschen curve as hypothesized by Graham and Roussel-Dupré. Experimental results yield no observable relativistic effects under the conditions of this experiment. Additionally, the collisional frequency limit has been experimentally identified.

TABLE OF CONTENTS

LIST OF FIGURES

LIST OF FIGURES (CONTINUED)

LIST OF TABLES

I. INTRODUCTION

Experiments at the Institute for Nuclear Science, Tomsk, Siberia, in the former USSR have demonstrated an interest in the ability to lase diatomic nitrogen via extremely short microwave pulses. In these experiments, lasing was achieved in N_2 at pressures less than or equal to one atmosphere[1,2,3]. Excitation of the gas was achieved with pulses which were approximately between 16 and 50 ns in duration. The frequency of the microwaves is reported to have been 3 GHz.

To lase gas with microwaves requires a knowledge of the Paschen curve, which is a graphical representation of the solution of the gaseous electrical breakdown equation. Breakdown is that condition in which the final electron density due to some form of excitation is 10^8 times the initial electron density. Knowledge of the Paschen curve allows estimates to be made of the required intensity of the electromagnetic field for a given pulse duration. Data in the region below 10^{-8} Torr-s with electromagnetic fields in excess of 10kV/cm/Torr had been unobtainable due to technical limitations. If accurate lasing research via microwave pumping is to be done in this region, experimental data must be obtained to either validate or repudiate current theory relating to this region. This document describes an

experiment preformed in this region.

Figure 1, see page 4, is a plot of the various Paschen curves of previous researchers available in the literature. The abscissa represents $P\tau_p$, which is the pulse duration multiplied by the operational pressure, while the ordinate represents E_o/P, which is the applied electromagnetic field divided by the operational pressure.

The first two lines on the upper right hand side of figure 1 are predications based on the theory of Ali and Coffey[4] for monofrequency microwave excitations of the upper atmosphere at 10 GHz and 3 GHz respectively. For this study Ali and Coffey assumed that the species from which ionization occurred was oxygen, which has a first ionization energy of 12.5 eV.

The third line from the top of the upper right hand side predicts that level above which breakdown must occur based on data acquired by Sullivan et al.[5] with monofrequency microwaves excitation of air at 9.6 GHz. Sullivan utilized a 10 to 200 kW/cm^2 gyrotron with pulses of between 3 and 30 ns.

The third line from the bottom left hand side is a prediction based on the theory of MacDonald[6] for monofrequency microwaves excitation air at 3 GHz.

The second line from the bottom left hand side is based on data acquired by Felsenthal and Proud[7] for a pulsed dc experimental system utilizing nitrogen as the working medium. The pulsed system was capable of generating a 4 to 30 kV pulse with rise times a short as 0.3 ns.

Finally, the bottom line on the left hand side is based on data acquired by Tetenbaum et. al.[8] which measured breakdown due to a pulsed S-band microwaves with pulse durations of between 100 to 600 ns. The pressure at which Tetenbaum operated varied from 1 to 1000 Torr.

The variation in the placement of the theories and the data over approximately two decades is due to the different media and different frequencies of investigations. Generally, higher frequencies reside closer to the upper right hand corner of figure 1. This is due to the effect of frequency on the calculation of the effective electric field. Higher frequencies tend to transfer less energy to an electron. Likewise, nitrogen gas tends to reside closer to the bottom left hand side of figure 1 with air and oxygen residing closer to the upper right hand side.

3

E₀/P (V/cm/Torr)

E_o/P (V/cm/Torr)

1e+06

100000

10000

1000

100

10
1e-10

1e-10   1e-09   1e-08   1e-07   1e-06   1e-05

P*t (Torr-s)
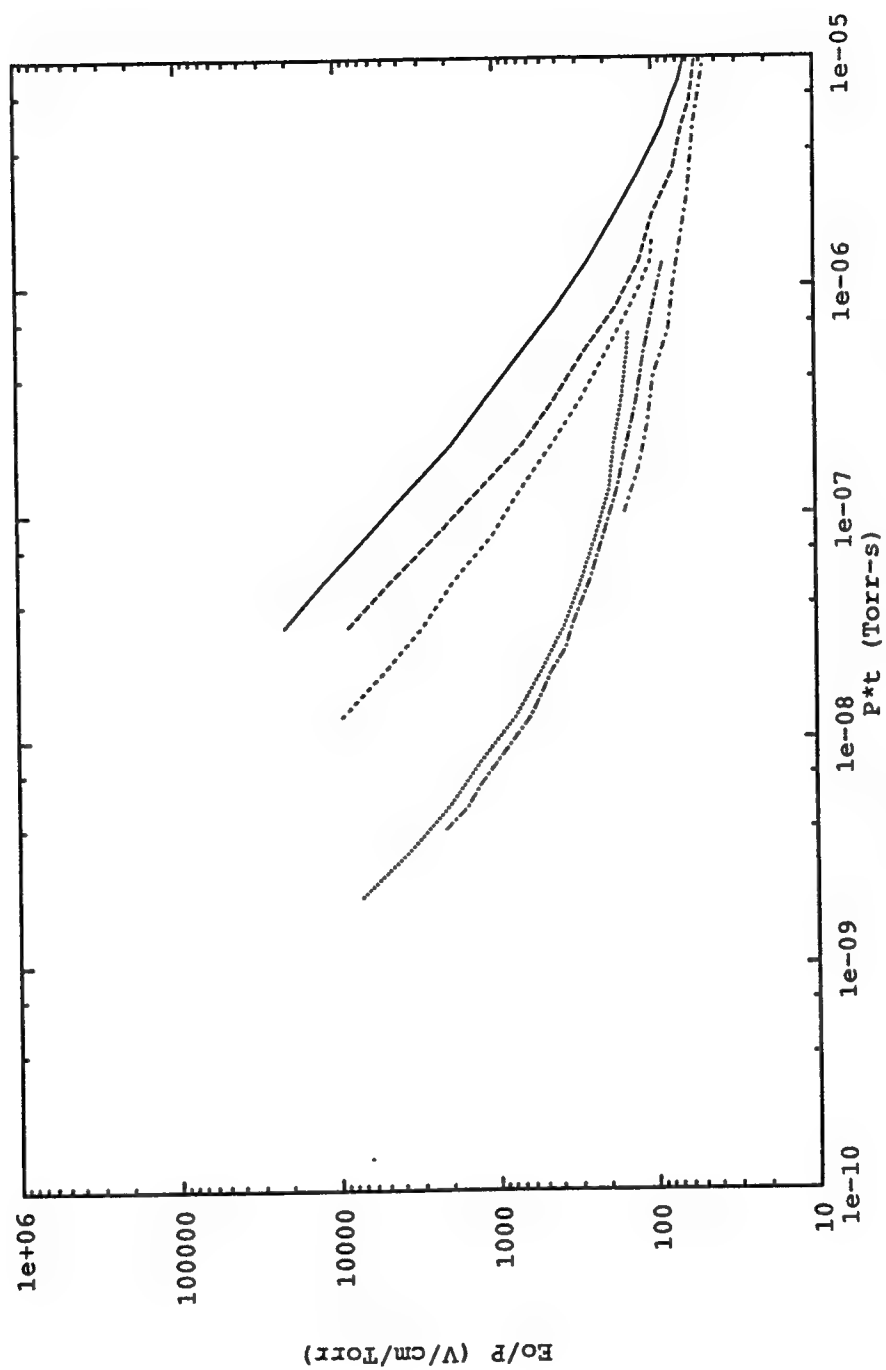
Figure 1.   Prior E_o/P vs. $P\tau_p$

Compilation of Previous Research

Figure 2 on page 7 is a plot of pressure versus pulse length compiled from a survey[1-22] of other research - R.F., spark gaps, etc. - relevant to this problem. The darkened areas are those which have been investigated, the boxed region is the area of interest to this investigation.

Utilizing a recently constructed pulse power device designated H-Two, it was possible to produce the required field strengths and pulse lengths necessary to perform this experiment. The H-Two device is capable of producing a 1.375 ns FWHM pulse of up to 720 kV across an open transmission line. Breakdown of nitrogen was achieved via excitation by broadband electromagnetic pulses, with a peak frequency content at approximately 200 MHz.

This investigation has examined the Paschen curve of nitrogen from pressures of 0.336 Torr to 685 Torr via the application of nanosecond pulsed electromagnetic radiation. This extends the efforts of earlier researchers by investigating the region in excess of 10 kV/cm/Torr for E_o/P and less than 10^{-8} Torr-s for $P\tau_p$, which had been experimentally denied due to technical limitations. An extensive literature search was unable to uncover any experimental data in this region.

The previous efforts utilized monofrequency sources, whereas

this effort utilized a broad band source with a frequency content peak at approximately 200 MHz. Since the results of Felsenthal and Proud were obtained for a pulsed D.C. experimental system, and the results of Ali and Coffey were calculated for 10 GHz and 3 GHz, the broadband signal to be bounded on the bottom by the work of Felsenthal and Proud, and on the top by the results of Ali and Coffey.
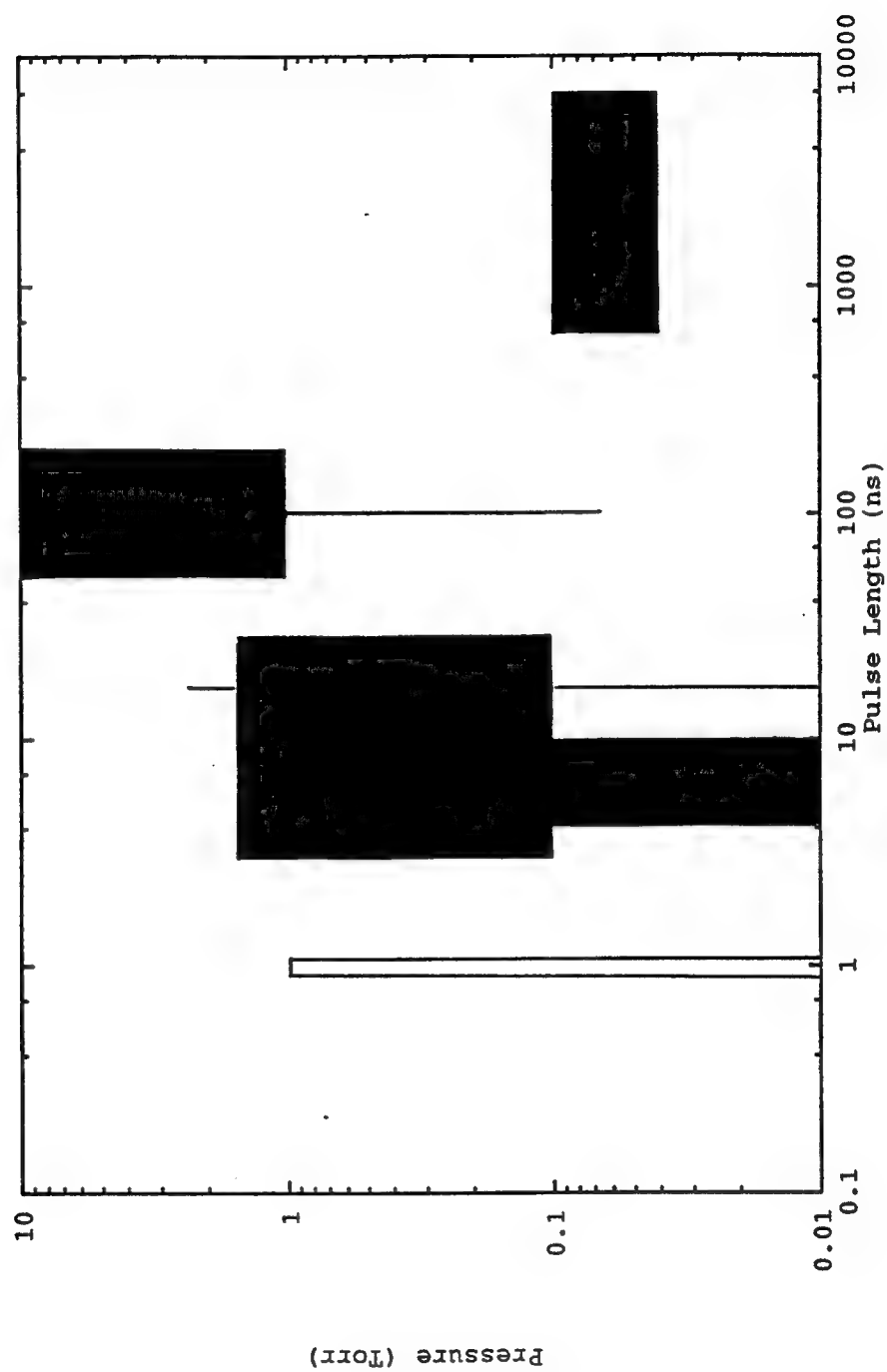
Figure 2. Pressure vs. Pulse Length Compilation

Investigation of the region in excess of 10 kV/cm/Torr for E_o/P and less than 10^{-8} Torr-s for $P\tau_p$ has yielded data in the regime of the relativistic Paschen Curve as theorized by Graham and Roussel-Dupré[23], see figure 3 on page 9. Graham and Roussel-Dupré developed the relativistic theory to describe phenomenon due to lightning in the upper atmosphere. The theory was developed assuming intense electromagnetic fields, with electron flow both perpendicular and parallel to the propagation of the electric field.

This document is divided into four sections. Section I, just presented, was the introduction, which discussed the motivation for this research, the previous investigations of prior researchers, and the uniqueness of this experimental investigation. Section II develops classical and relativistic theories for broadband electromagnetic radiation, extending previous classical theories for monofrequency electromagnetic sources. Section III describes the pulse power device used to generate the broadband electromagnetic pulse, the test chamber, and the diagnostics used to monitor the pulse. Section III continues with a discussion of the procedure to acquire the data, the process used to reduce the data, and the analysis performed on the data. Finally, Section IV presents the conclusions derivable from the analysis performed on the data.
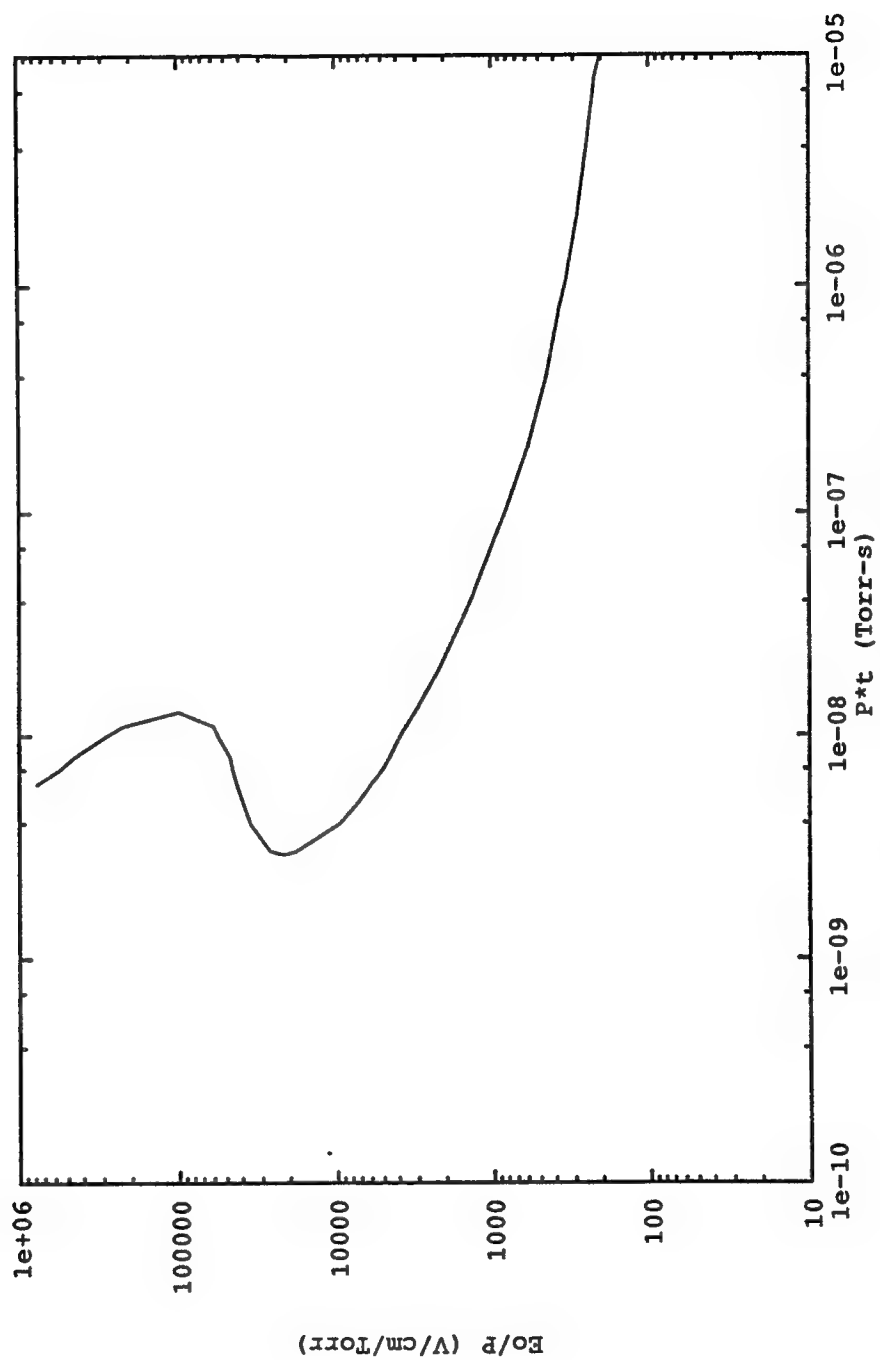
Figure 3. Relativistic E_o/P vs. $P\tau_p$

II A. CLASSICAL THEORY

This section develops classical theory for broadband electromagnetic radiation. This development represents an extension to current theories, which have been developed predominately for monofrequency electromagnetic excitation.

For nanosecond pulsed electromagnetic radiation, minor adjustments to monofrequency classical theory must be made. As has been shown by previous authors[5-7,24], the equation which governs the time rate of growth of breakdown is the continuity equation,

$$\frac{\partial n}{\partial t} = v_i n - v_a n + \nabla^2 (Dn) \qquad (1)$$

where: n = electron density

v_i = ionization rate

v_a = attachment rate

D = electron diffusion coefficient

When an electromagnetic pulse is short compared to the diffusion time, the electron diffusion coefficient may be neglected[6]. This allows equation 1 to be rewritten as

$$\frac{\partial n}{\partial t} = \Delta v n \qquad (2)$$

where: $\Delta v = v_i - v_a$

10

Solving equation 2, assuming Δv is not a function of time, yields

$$\ln\frac{n_f}{n_o} \approx \Delta v \tau_p \qquad (3)$$

where: n_f = final electron density

n_o = initial electron density

τ_p = pulse length

Gould and Roberts[25] established the generally recognized breakdown ratio of n_f/n_o as 10^8.

$$\ln 10^8 = 18.4 \approx \Delta v \tau_p \qquad (4)$$

For breakdown to occur it is required that $v_i \gg v_a$. Thus

$$\frac{v_i}{P} = \frac{18.4}{P\tau_p} \qquad (5)$$

where: P = gas pressure

Following the development of Lupan[26], the functional dependence of the ratio of v_i/P to E_{eff}/P can be derived.

11

The average value of this ratio is

$$\langle \frac{v_i}{P} \rangle = \frac{N}{P} \langle \sigma(E) \sqrt{\frac{2E}{m_e}} \rangle \tag{6}$$

where: N = gas density

$\sigma(E)$ = collisional cross section of the gas molecule

E = energy

m_e = electron mass

$\langle \sigma(E) * [2E/m_e]^{1/2} \rangle$ = average collisional rate

coefficient integrated over a distribution function.

Assuming a Maxwellian distribution for E,

$$\langle \frac{v_i}{P} \rangle = \int_{E_i}^{\infty} \frac{N}{P} \sigma(E) \sqrt{\frac{2E}{m_e}} \frac{2}{\sqrt{\pi}} \sqrt{\frac{E}{\frac{2}{3}\varepsilon}} \exp\{\frac{-3E}{2\varepsilon}\} \frac{dE}{[\frac{2}{3}\varepsilon]} \tag{7}$$

where[26]

$$\varepsilon = \frac{3}{2} k_B T + \frac{Q^2 E_{eff}^2}{m_e \delta_{eff} v_{eff}^2}$$

and k_B = Boltzmann's constant,

T = temperature,

Q = electron charge,

E_{eff} = effective E-field,

δ_{eff} = effective fraction of energy transferred

from an electron to a molecule in a

collision,

v_{eff} = effective collision frequency,

12

Equation 7 can be rewritten as

$$\langle \frac{v_i}{P} \rangle = \frac{2}{\sqrt{\pi}} \sqrt{\frac{3}{2\varepsilon}} \frac{3}{2\varepsilon} \int_{E_i}^{\infty} \frac{N}{P} \sigma(E) \sqrt{\frac{2E}{m_e}} \sqrt{E} \exp\{\frac{-3E}{2\varepsilon}\} dE \qquad (8)$$

here E_i is the first ionization potential of nitrogen. The functional dependence of the first three terms contained in the integral can be estimated[26] for the field values of this investigation based on data of the ionization cross section of nitrogen, and assuming that ionization is a single event process. For $E \leq 400$ eV this estimate yields,

$$\frac{N}{P} \sigma(E) \sqrt{\frac{2E}{m_e}} = 6 \times 10^7 \alpha \sqrt{E} (E-E_i) \exp(\frac{E_i-E}{\beta_{N2}}) \qquad (9)$$

where[27]: $\alpha = 0.2$ cm^{-1} Torr^{-1}

$\beta_{N2} = 142.5$ eV

$E_i = 15.5$ eV

For $E > 400$ eV, the functional dependence of the first three terms contained in the integral are estimated to be

$$\frac{N}{P} \sigma(E) \sqrt{\frac{2E}{m_e}} = \frac{6 \times 10^7 \sqrt{E}}{\sqrt{E}} 10^2 = 6 \times 10^9 \qquad (10)$$

13

Substituting equations 9 and 10 into equation 8 yields,

$$\langle \frac{V_i}{P} \rangle = 6 \times 10^7 \sqrt{\frac{27}{2\pi}} \; \varepsilon^{-3/2} \, [\alpha \int_{E_i}^{400} E(E-E_i) \exp\{\frac{E_i-E}{\beta_{N2}}\} \exp\{\frac{-3E}{2\varepsilon}\} dE +$$

$$10^2 \int_{400}^{\infty} \sqrt{E} \exp(\frac{-3E}{2\varepsilon}) \, dE] \qquad (11)$$

Performing the integration (refer to appendix A) and combining with equation 5 yields

$$\frac{18.4}{P\tau_p} =$$

$$6 \times 10^7 \sqrt{\frac{27}{2\pi}} \; \varepsilon^{-3/2} \{ \frac{2\alpha\beta_{N2}\varepsilon}{2\varepsilon+3\beta_{N2}} \; [\frac{8(\beta_{N2}\varepsilon)^2}{(2\varepsilon+3\beta_{N2})^2} + \frac{4\beta_{N2}\varepsilon E_i}{2\varepsilon+3\beta_{N2}} + E_i^2] \exp(\frac{-3E_i}{2\varepsilon})$$

$$- \frac{2\alpha\beta_{N2}\varepsilon E_i}{2\varepsilon+3\beta_{N2}} \; (\frac{2\beta_{N2}\varepsilon}{2\varepsilon+3\beta_{N2}} + E_i) \exp(\frac{-3E_i}{2\varepsilon})$$

$$+10^2 \sqrt{\frac{2\pi\varepsilon}{3}} \exp(\frac{-600}{\varepsilon}) (\frac{2\varepsilon}{3}+800) \} \qquad (12)$$

14

Which reduces to

$$\frac{18.4}{P\tau_p} =$$

$$6x10^7 \sqrt{\frac{27}{2\pi}}\, \varepsilon^{-3/2} \exp\left(\frac{-3E_i}{2\varepsilon}\right)\left\{\frac{16\alpha(\beta_{N2}\varepsilon)^3}{(2\varepsilon+3\beta_{N2})^3} + \frac{4\alpha(\beta_{N2}\varepsilon)^2 E_i}{(2\varepsilon+3\beta_{N2})^2}\right.$$

$$\left. +10^2 \sqrt{\frac{2\pi\varepsilon}{3}}\, \exp\left(\frac{3E_i-1200}{2\varepsilon}\right)\left(\frac{2\varepsilon}{3}+800\right)\right\} \tag{13}$$

For $\varepsilon<<\beta_{N2}$, the above solution approximately yields

$$\frac{18.4}{P\tau_p} = 6x10^7 \sqrt{\frac{27}{2\pi}}\, \varepsilon^{-3/2} \exp\left(\frac{-3E_i}{2\varepsilon}\right)\left\{\frac{16\alpha\varepsilon^3}{27} + \frac{4\alpha\varepsilon^2 E_i}{9}\right.$$

$$\left. +10^2 \sqrt{\frac{2\pi\varepsilon}{3}}\, \exp\left(\frac{-1200+3E_i}{2\varepsilon}\right)\left(\frac{2\varepsilon}{3}+800\right)\right\} \tag{14}$$

For $\varepsilon\approx\beta_{N2}$, equation 13 yields

$$\frac{18.4}{P\tau_p} = 6x10^7 \sqrt{\frac{27}{2\pi}}\, \varepsilon^{-3/2} \exp\left(\frac{-3E_i}{2\varepsilon}\right)\left\{\frac{16\alpha\varepsilon^3}{125} + \frac{4\alpha\varepsilon^2 E_i}{25}\right.$$

$$\left. +10^2 \sqrt{\frac{2\pi\varepsilon}{3}}\, \exp\left(\frac{-1200+3E_i}{2\varepsilon}\right)\left(\frac{2\varepsilon}{3}+800\right)\right\} \tag{15}$$

15

For $\varepsilon \gg \beta_{N2}$ and E_i, equation 13 approximately yields

$$\frac{18.4}{P\tau_p} = 6x10^7\sqrt{\frac{27}{2\pi}} \, \varepsilon^{-3/2}\exp\left(\frac{-3E_i}{2\varepsilon}\right)\{2\alpha\beta_{N2}^3 + \alpha\beta_{N2}^2 E_i$$

$$+10^2\sqrt{\frac{2\pi\varepsilon}{3}} \exp\left(\frac{-1200+3E_i}{2\varepsilon}\right)\left(\frac{2\varepsilon}{3}+800\right)\} \tag{16}$$

Recall that,

$$\varepsilon = \frac{3}{2}k_B T + \frac{Q^2 E_{eff}^2}{m_e \delta_{eff} v_{eff}^2} \tag{17}$$

This discussion will assume[6] that $v_{eff}=5.3x10^9 P$ where v_{eff} has units of s^{-1} and P has units of Torr, and from Appendix B that $E_{eff}=0.310E_o$ for the area of interest for this investigation. Observing that the average electron energy in a microwave discharge is much greater than $(3/2)k_B T$, that $m_e = 9.11x10^{-28}$ gm, and that[26] $\delta_{eff}=1.3x10^{-2}$, equation 17 yields

$$\varepsilon = \frac{(0.310)^2(1.602x10^{-19})10^7}{1.3x10^{-2}(5.3x10^9)^2(9.11x10^{-28})}\left(\frac{QE_o}{P}\right)^2$$

$$\varepsilon = 4.63x10^{-4}\left(\frac{QE_o}{P}\right)^2 \tag{18}$$

Equation 13 is plotted in figure 4 on page 18 with the substitution of equation 18, and the values: α=0.2 cm^{-1} Torr^{-1}, β_{N2}=142.5 eV, and E_i=15.5 eV. The ordinate represents E_o/P while the abscissa represents $P\tau_p$. The graph of this Paschen curve demonstrates a departure from the traditional monofrequency curves of previous researchers. At approximately 1×10^{-9} Torr-s and 1000 V/cm/Torr the Paschen curve reverses and transitions to the collisional frequency limit. The features of reversal and transition to the collisional frequency limit have not been addressed in the Paschen curve investigations of previous researchers.
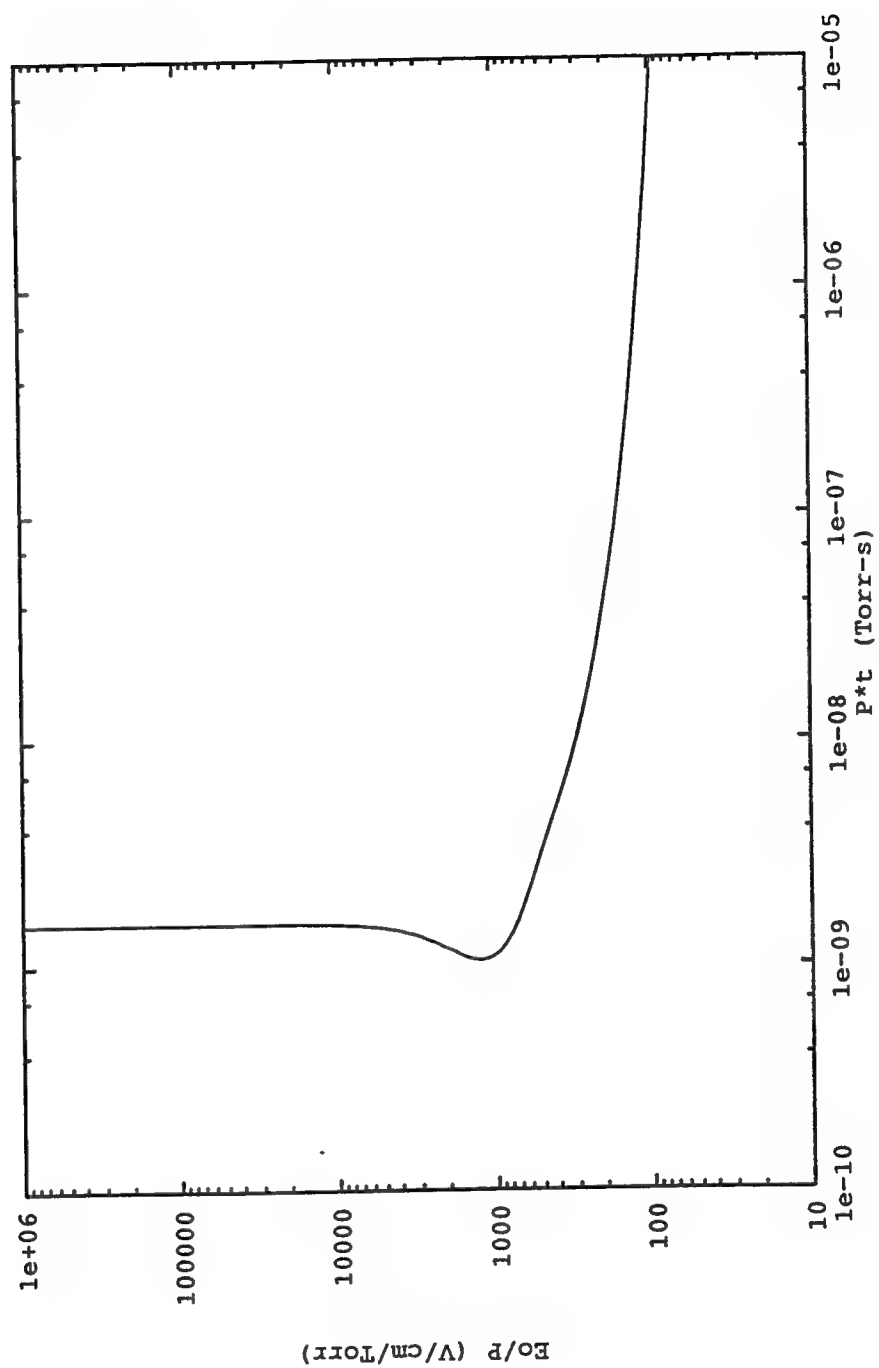
Figure 4. Classical E_o/P vs. $P\tau_p$

18

II B. RELATIVISTIC THEORY

This section describes, in brief, the relativistic theory of Graham and Roussel-Dupré and then develops a one dimensional theory for intense electric fields, utilizing classical scattering theory with relativistic corrections.

Scattering at classical energies allows the electric fields of the incoming particles to be treated as isotropic fields (see figure 5 below).
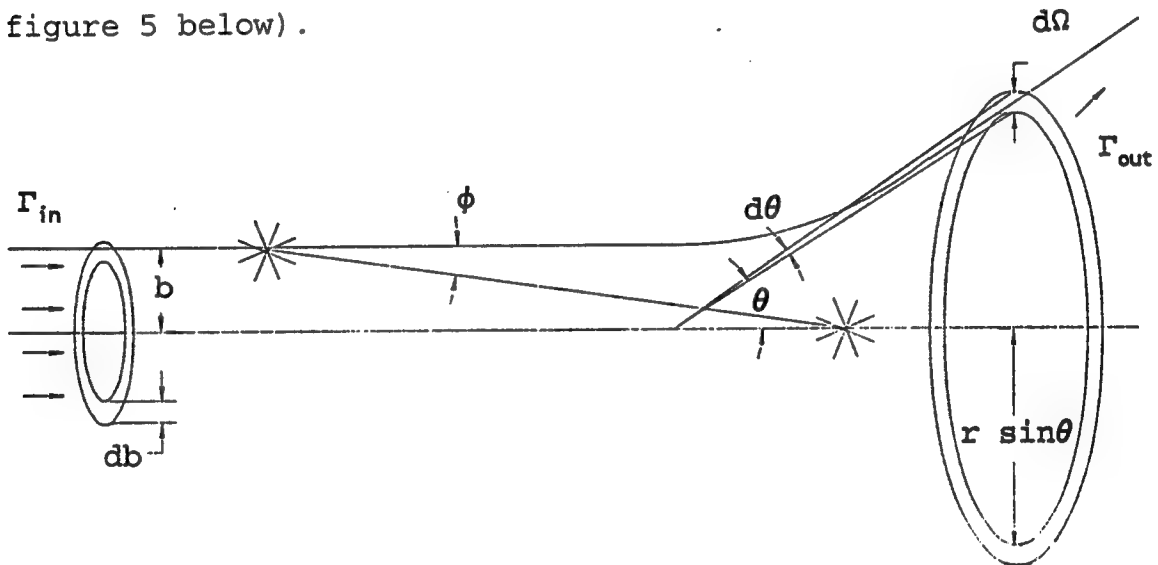
Figure 5. Classical Scattering.

Under the influence of intense electromagnetic fields a free electron is capable of obtaining a velocity sufficient to exhibit relativistic effects[28]. When this occurs, the electric field of the incoming relativistic particle redistributes itself, as seen by the scattering center (fixed frame).

The equation describing this redistribution is

$$E = \frac{Q}{R^2\gamma^2 (1-\beta_{rel}^2\sin^2\phi)^{3/2}}$$

Where: Q = Electron charge $(1.6\times10^{-19}$ C)

R = charge separation

β_{rel} = v/c

$\gamma = [1 - \beta_{rel}^2]^{-1/2}$

The field is in the radial direction, but the electric lines of force are distributed isotropically only when $\beta_{rel}\approx0$. For $\beta_{rel}\neq0$, the electric force is reduced by a factor of γ^2 when viewed along the axis of motion, while when viewed perpendicular to the axis of motion the electric field is increased by a factor of γ. This effect is shown in figure 6 for $\gamma\approx1$ and $\gamma\approx3$ on page 21, with the magnitude of the electric field represented by line length. Under this influence the effective collision frequency has been shown[35] to be

$$\nu_{eff}\tau_p = \frac{\nu}{1-\beta_{rel}}$$

Noting equation B-1 of appendix B it is seen that the effective E-field is a function of the effective collision frequency.

$$E_{eff} = \frac{E}{[2(1+\frac{\omega^2}{\nu_{eff}^2})]^{1/2}}$$
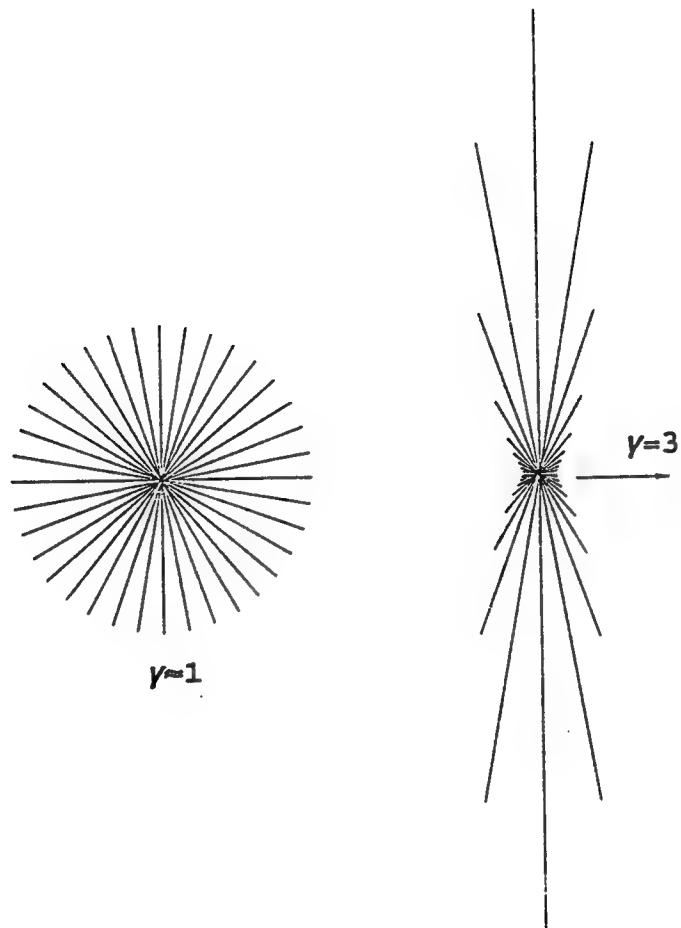
Figure 6.   Electric Field Distribution.

$\gamma \approx 1$ and $\gamma \approx 3$

Thus the relativistic ratio β_{rel} is a function of E_{eff}/P, which itself is a function of ν_{eff}, which in turn is a function of β_{rel}. Thus an existential/transcendental set of equations must be solved. This problem has been addressed via a numerical approach by Graham and Roussel-Dupré[23] for air. Figure 7, on page 23, is a plot of the Paschen curve derived by Graham and Roussel-Dupré based on their numerical approach. The ordinate represents E_o/P in V/cm/Torr while the abscissa represents $P\tau_p$ in Torr-s. The solid line represents the relativistic Paschen curve for air. Features of interest include the reversal of the curve from 1×10^4 V/cm/Torr to 2×10^4 V/cm/Torr, and the reestablishment of the curve above 3×10^5 V/cm/Torr. The hypothesis put forth by Graham and Roussel-Dupré as to the cause of this reversal is that as an electron achieves higher velocities the electric field of the electron becomes redistributed, as viewed in the laboratory frame, due to Lorentz contraction. As the electron achieves velocities approximately equal to the velocity of light the redistribution becomes essentially fixed, that is to say that additional energy added to the electron can no longer provide as great an acceleration as before, and the Paschen curve reestablishes the original behavior.
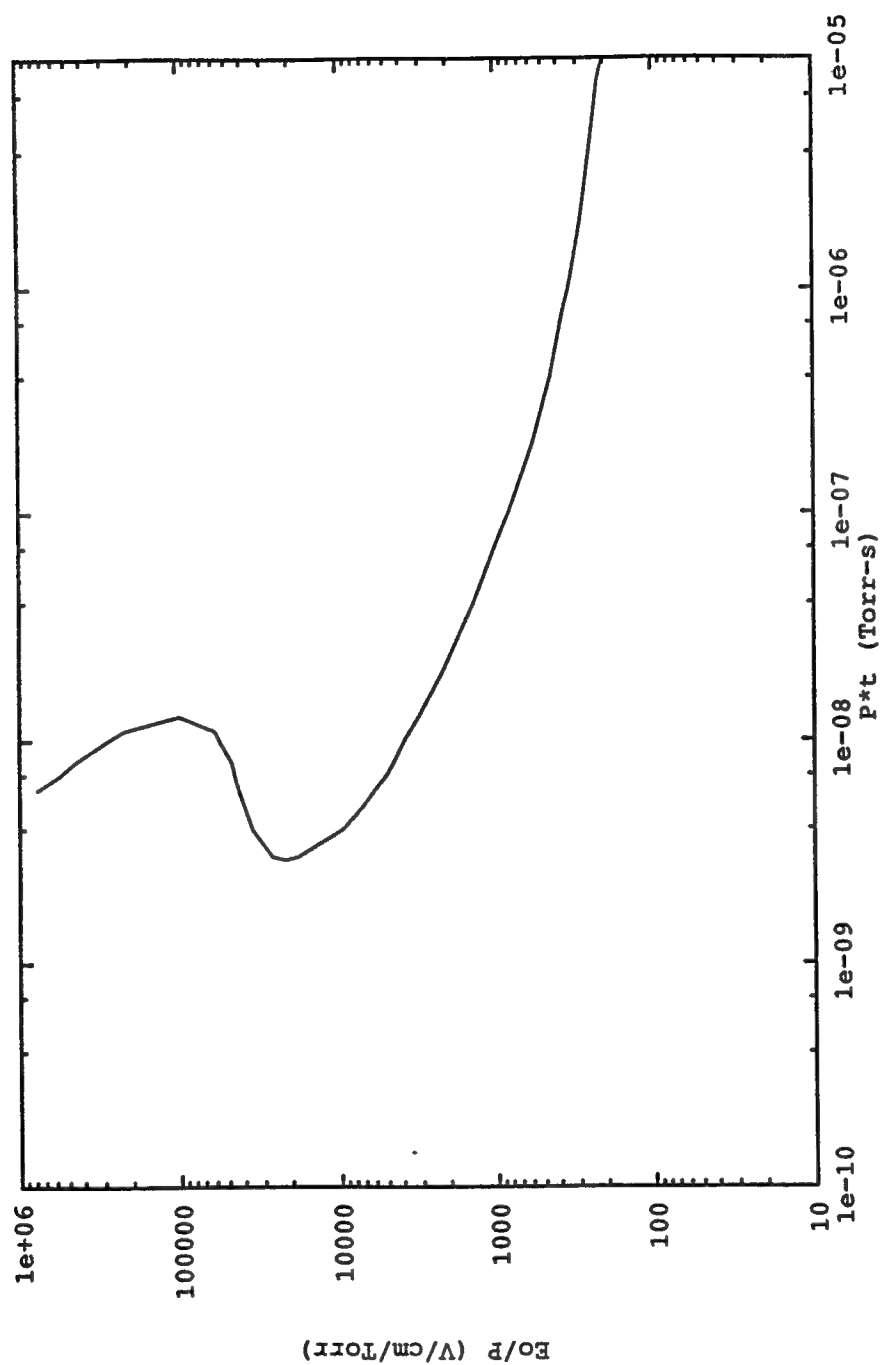
Figure 7. Relativistic E_o/P vs. $P\tau_p$

(After Reference 23)

The Paschen curve derived by Graham and Roussel-Dupré assumed intense E-fields, B-fields, and electron flow in two dimensions. The experimental configuration of this investigation only allowed intense E-fields with electron flow in one dimension. This necessitated extension of the classical theory into the relativistic domain. Appendix C develops a relativistic derivation of the Paschen curve beginning from first principles. The results of this derivation are presented in figure 8 on page 25. The ordinate represents E_o/P in V/cm/Torr while the abscissa represents $P\tau_p$ in Torr-s. The solid line represents the relativistic Paschen curve for air, the long dashed line represents the classical curve for nitrogen, the short dashed line represents the relativistic curve for nitrogen as derived in Appendix C. Note that all three theories produce a reversal in the paschen curve. In the classically derived theory the reversal transitions into a vertical barrier. In the relativistic theory of Graham and Roussel-Dupré the reversal transitions through yet another reversal to reestablish the Paschen curve at a higher value of E_o/P. The relativistic theory developed in Appendix C produces a reversal which continues into the upper right hand quadrant of the plot, which is attributed to the one dimensional nature of the theory (Refer to Appendix C for details).

24
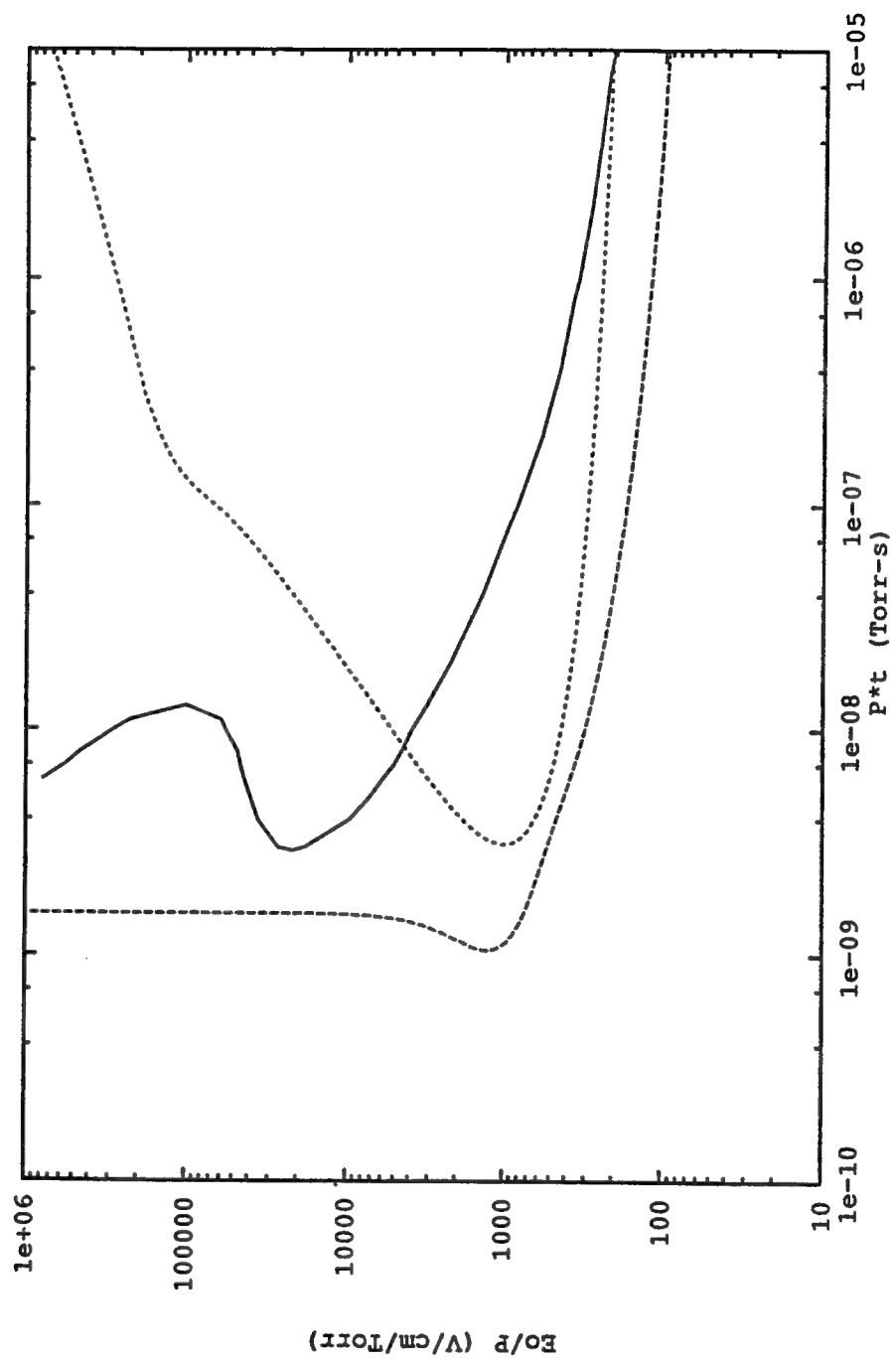
Figure 8. Comparison of Theories

25

The H-Two device, to be discussed in the Experimental Configuration section, has produced electromagnetic pulses as part of this investigation capable of exploring the region below 10^{-8} Torr-s with electromagnetic fields in excess of 10kV/cm/Torr. The results of this investigation follow.

III A. EXPERIMENTAL CONFIGURATION

Section III describes the H-Two pulse power device used to generate the broadband electromagnetic pulse, the test chamber in which the discharge occurred, and the diagnostics used to monitor the event. This section continues with a discussion of the data acquisition procedure, the process used to reduce the data, and the analysis performed on the data.

The H-Two pulse power device was used to provide the transient electromagnetic events. A schematic of this device is shown in figure 9.
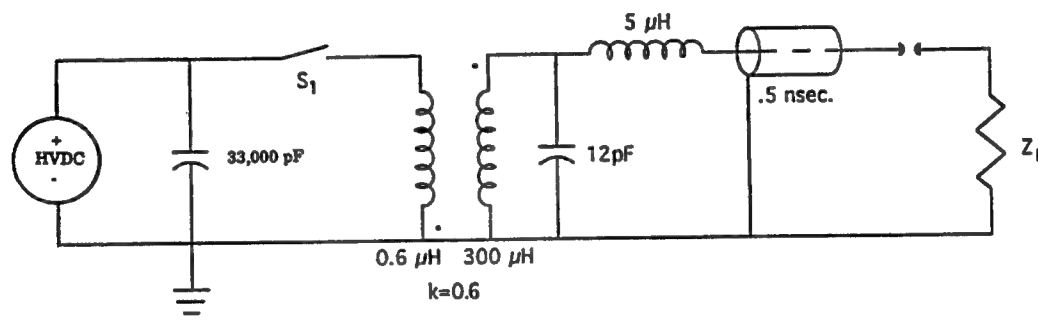
Figure 9. H-Two Schematic

This device is capable of developing a 1 J, 1.375 ns FWHM pulse of up to 360 kV into a 50 Ω load, or 720 kV into an open circuit. A typical oscilloscope trace is shown in figure 10 on page 28. The abscissa is time in nanoseconds while the ordinate is volts. Visible is the rising edge of the pulse, the occurrence of breakdown, the ringing of the circuit after the arc, and the exponential decay envelope.

27
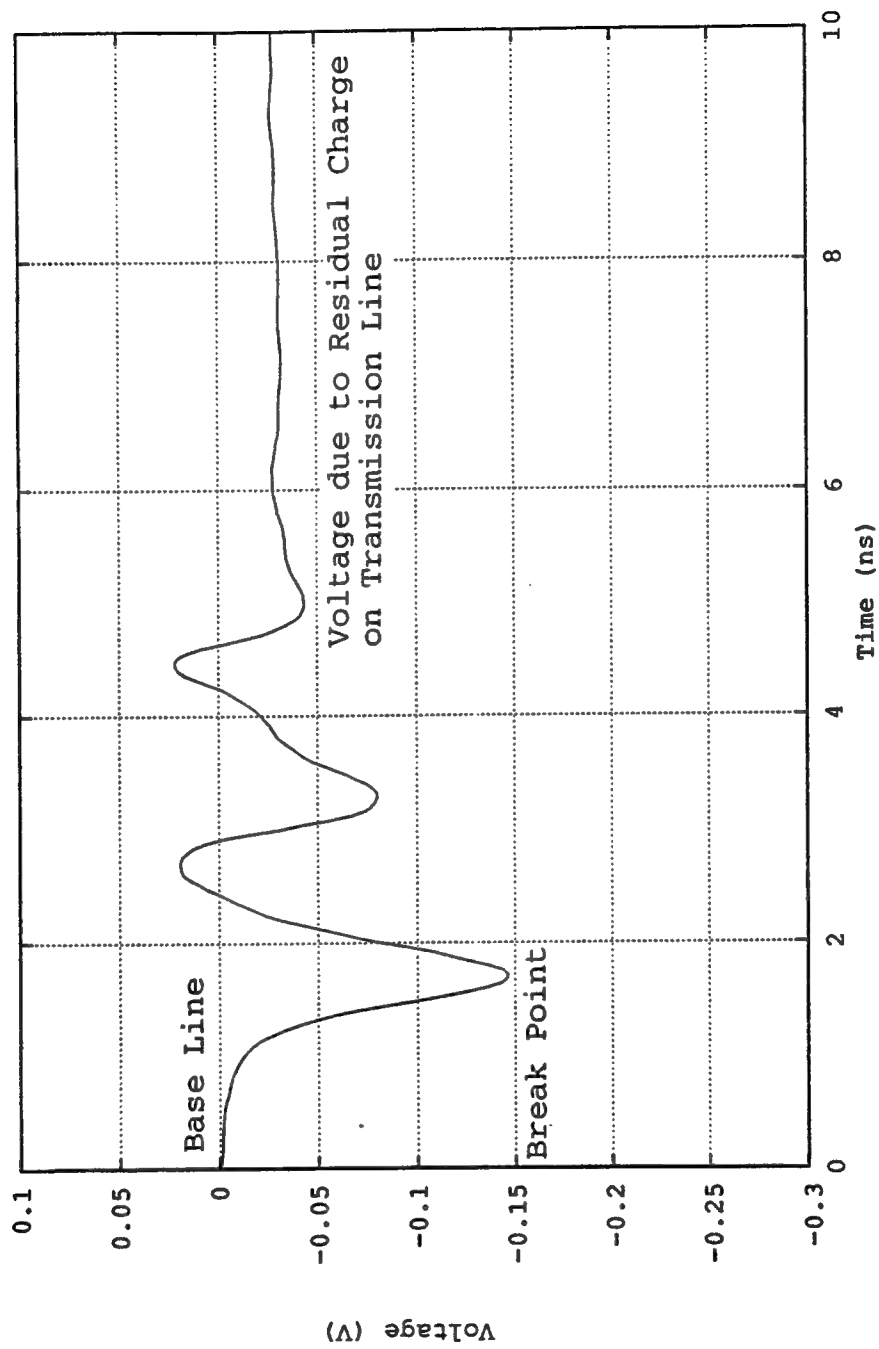
Figure 10. H-Two Pulse Profile.

Figure 11 on page 30 is a plot of a hypothetical 1 ns duration triangular pulse with a peak amplitude of 1 MV at a pressure of 10 Torr. The abscissa is Torr-s while the ordinate is V/cm/Torr. The solid line represents the relativistic Paschen curve while the dashed line represents the track of the pulse. This plot demonstrates that a machine with H-two's performance can investigate the nose region of the relativistic Paschen curve.

The high voltage power supply was a Hippotronics Labtrol capable of 25 kV charge. Triggering was provided by a Maxwell Laboratories, Inc. 40127-B Trigger Channel, which in turn drove a Northstar Research Corp. Thyratron Driver, and an Optical Multichannel Analyzer. The thyratron driver provided the trigger to the thyratron switch between the capacitors and the primary inductor as shown in the schematic.

A transparent test chamber capable of pressures from 100 mTorr to 7600 Torr (gauge) was constructed, and clamped directly to the H-Two device. The chamber was a 76 cm long, 30 cm I.D. plexiglass tube with a thickness of 2.54 cm. The end through which the transmission line entered the test chamber was sealed with a 2.54 cm thick aluminum bulkhead. The end at which the parallel plate transmission line terminated was
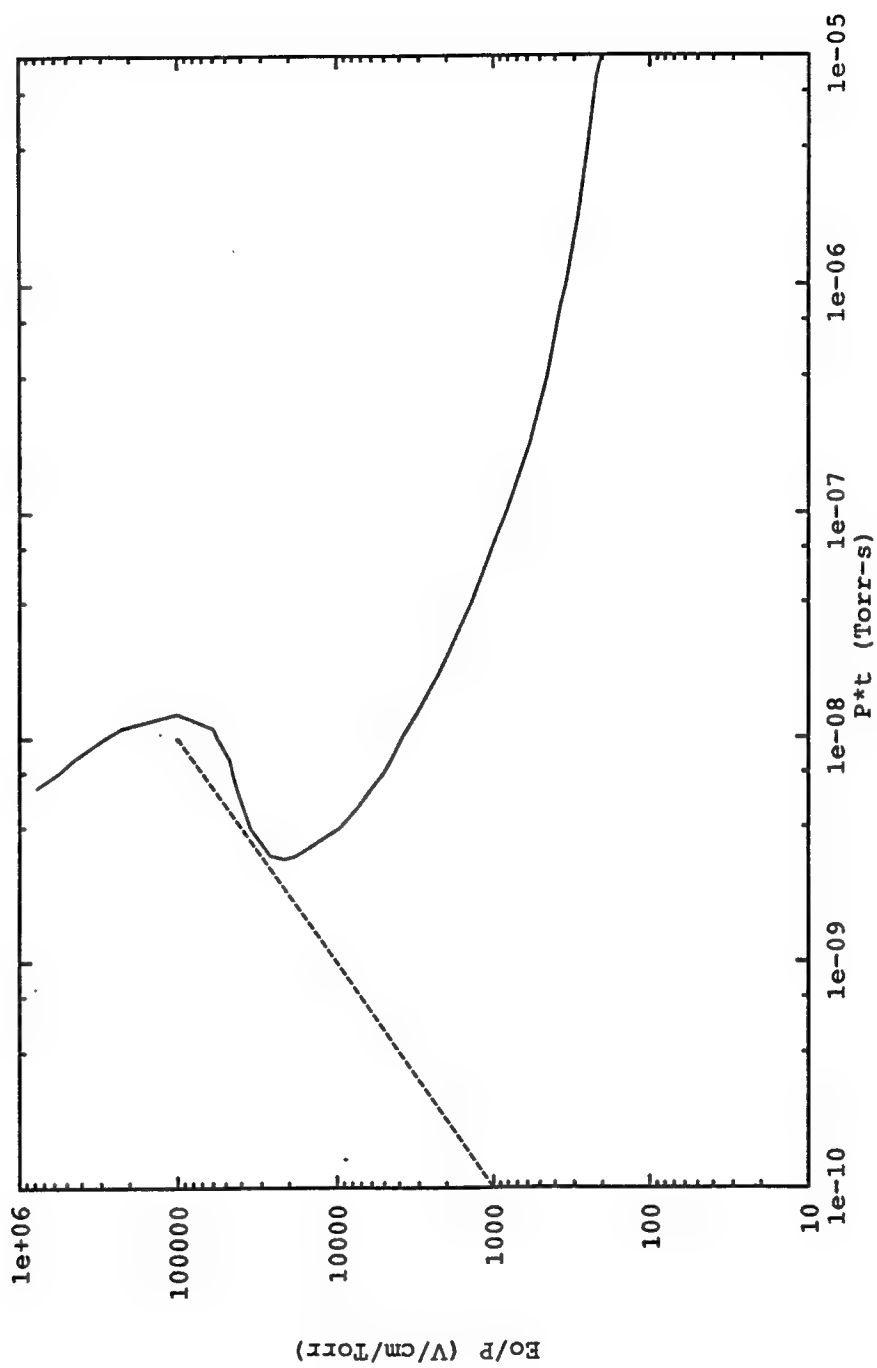
Figure 11. Triangular Pulse Track.

30

sealed with a 4.78 cm thick plexiglass bulkhead and a 5.08 cm
plexiglass access panel. See figure 12.
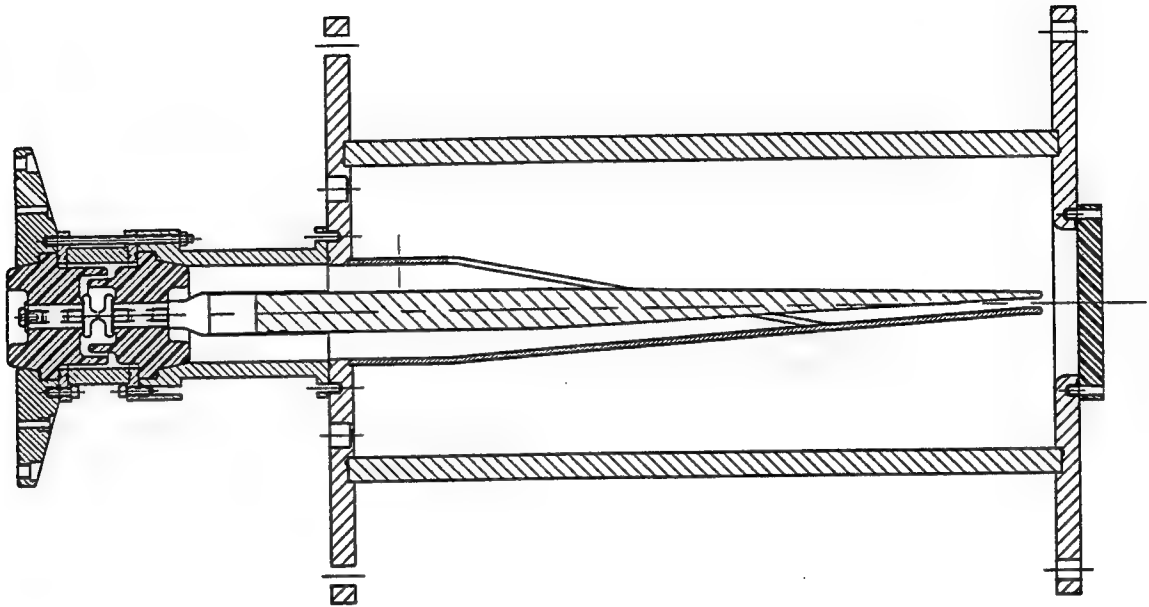
Figure 12. Test Chamber.

The chamber contained a section transitioning from the 50 Ω
coaxial transmission line to the parallel plate transmission
line. The lower plate of the parallel plate transmission line
was the electrical ground. Two center conductors were
machined for the experiment. A 7.23 cm wide center conductor
was manufactured to produce a parallel plate transmission line
with an impedance of 50 Ω at a 1 cm AK gap. A 1 cm wide
tapered center conductor was manufactured to produce a
parallel plate transmission line with an impedance of 50 Ω at
a 0.14 cm AK gap.

31

The data acquisition system (see figure 13 on page 33) consisted of a Zenith-248 286 computer equipped with a National Instruments, Inc. PC2A GPIB board. The software used to operate the data acquisition system was DCS01, version 2.05, by Tektronix, Inc. The 286 computer was connected via the GPIB board to a Tektronix, Inc MUX 16 Multiplier. The mux box was required so that the software could communicate with three DCS01 cameras. The cameras were mounted on the front of three Tektronix 7103 oscilloscopes. The 7103 oscilloscopes were equipped with 7A29 preamps, and 7B10 time bases to provide 1 GHz bandwidth and 0.35 ns risetime capability for signal diagnostics.

Optical diagnostics were provided by an E.G.&G. Princeton Applied Research Model 1460 Optical Multichannel Analyzer III. The OMA was used to verify that a N_2 spectrum was being produced by the discharge. The optical data was acquired via two lengths of ultra violet rated Mitsubishi ST-U200D-FV fiber optic cable. A 25 m long cable viewed the discharge perpendicular to the arc while a 50 m long cable viewed the discharge down the axis of the arc.

32
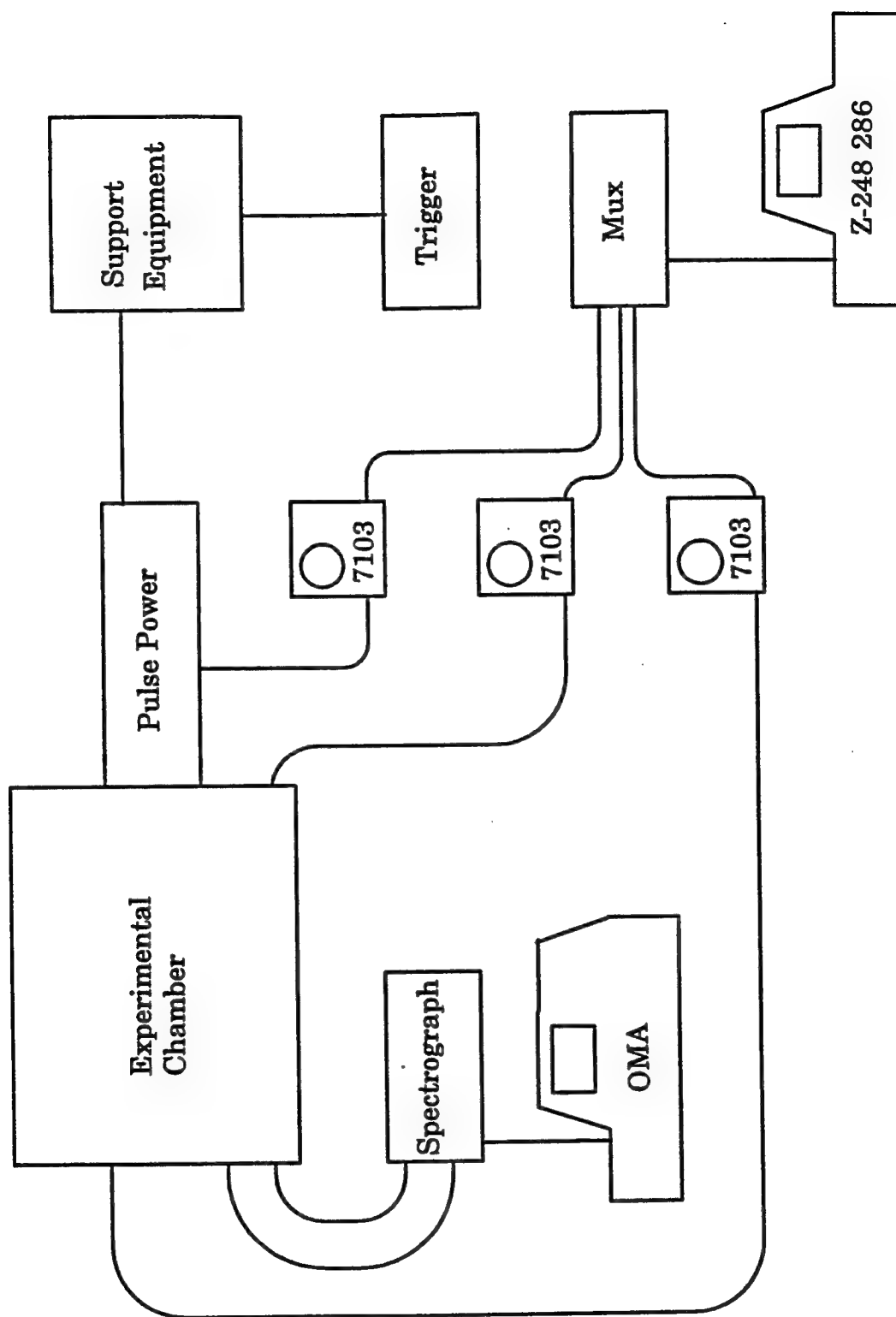
Figure 13. DAS Block Diagram.

33

The data lines consisted of five RG-214 cables, with N-type connectors, running from the screen room to the experimental area. Inside the screen room the cables transitioned to 152.4 cm long RG-141 cables with SMA connectors. At the experimental area, additional lengths of RG-214 were attached to the cables to provide a transition from the experimental area patch panel to the experimental device. All data lines were then measured for attenuation characteristics and electrical length. Since the coaxial lines were operating in TEM mode dispersion was negligible. The three data lines most closely matched in electrical length, and with the best match to the theoretical attenuation curve, were selected as the primary data lines for the pulse power diagnostic, transmission line sensor, and the tip sensor. Of the two remaining data lines, one was utilized as a trigger line for the thyratron drive while the other was left idle to provide a backup in the event of a failure.

Pressure inside the test chamber was sensed by two Granville-Phillips 275 Convection Gauges and by one Varian 865 gauge equipped with a 0536 vacuum transducer. This duality provided for a cross-check to ensure that the gauges were functioning properly.

The pulse power switch sensor consisted of copper clad RG-141 with the center conductor extending 0.165 cm radially inward from the outside wall of the gaseous switch.   See figure 14.

RG-141 Center Conductor

Ground Plane

Brass Housing
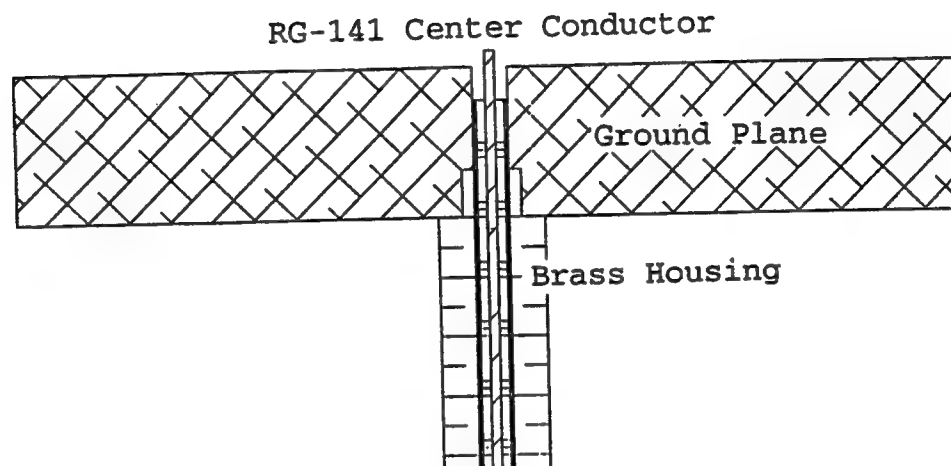
Figure 14.   Pulse Power Switch Sensor.

The outside wall represented electrical ground and was in electrical contact with the copper outer conductor of the probe.   This allowed the sensor to function as a half wave dipole antenna at a frequency of approximately 45 GHz. Equipment to provide a rigorous calibration of the pulse power switch sensor was not available.   Therefore an estimate of the sensor's signal coupling ability was calculated based on the geometry of the gaseous switch.   The gap from the switch channel to the grounded wall containing the sensor was 8.839 cm in length.

Attenuation due to geometrical considerations is

$$20\log\frac{8.839}{0.165}=34.5dB$$

Attenuation due to a mismatch between the transmission line impedance and the pulse power switch sensor radiation resistance, R_a, must also be accounted for. The radiation resistance for an infinitesimal dipole antenna has been calculated to be[29]

$$R_a=80\pi^2\left(\frac{l}{\lambda}\right)^2$$

which for the geometries and wavelengths under consideration yields

$$R_a=80\pi^2\left(\frac{0.065}{59.0}\right)^2=0.00096\Omega$$

Since the transmission line and the data cable are both 50 Ω it is necessary to account for reflections at both interfaces. The voltage reflection coefficient, Γ, is

$$\Gamma=\frac{0.00096-50}{0.00096+50}=-0.99996$$

This yields a functional attenuation of 0 dB at each interface. The total estimate for the attenuation of the pulse power switch sensor is 34.5 dB.

The transmission line sensor consisted of a capacitative probe
of approximately 2200 pF, constructed with a 2.54 cm diameter
disk of silver coated 0.0005 cm thick mylar (see figure 15
below). The probe was recessed 0.737 cm into the wall of the
50 Ω coaxial transmission line. Equipment to provide a
rigorous calibration of the transmission line sensor was not
available. As this sensor was used as a qualitative health
check of the pulse power device, a rigorous attenuation
estimate was not pursued.

**Silver Coated
0.0005 Mylar Film**

**Brass
Housing**

Ground Plane

RG-141
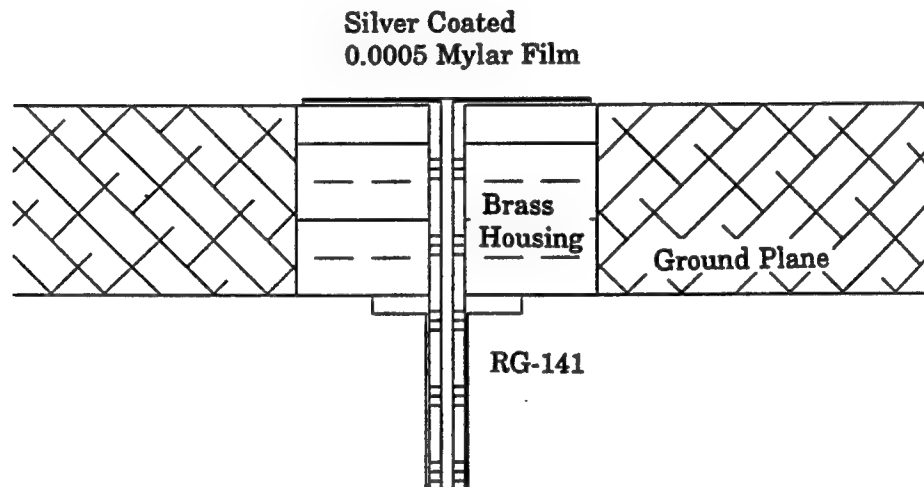
Figure 15. Transmission Line Sensor.

The tip sensor consisted of an SMA bulkhead feedthrough jack receptacle. A fiber optic port, for the optical verification of an N_2 spectrum, consisted of a SMA jack to jack bulkhead adapter which had the insulator and center conductor bored out (see figure 16).
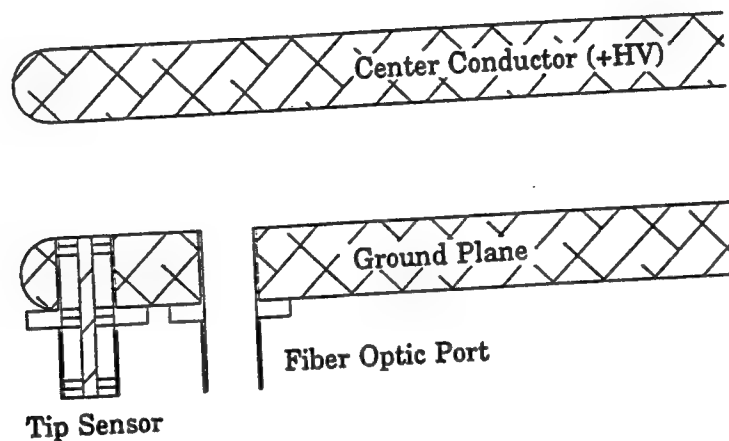
Figure 16. Tip Sensor.

The tip sensor was mounted at the tip of the ground plane of the 50 Ω flat plate transition. The sensor was mounted such that its open end was flush with the upper surface of the ground plane.

The assembly with the 7.23 cm wide center conductor and 1 cm wide center conductor was then calibrated for coupling and phase effects with an HP 8510 vector network analyzer. Overall, the coupling coefficient had an attenuation of approximately -25 dB (see figures 17 and 18 on pages 39 and 40 respectively).
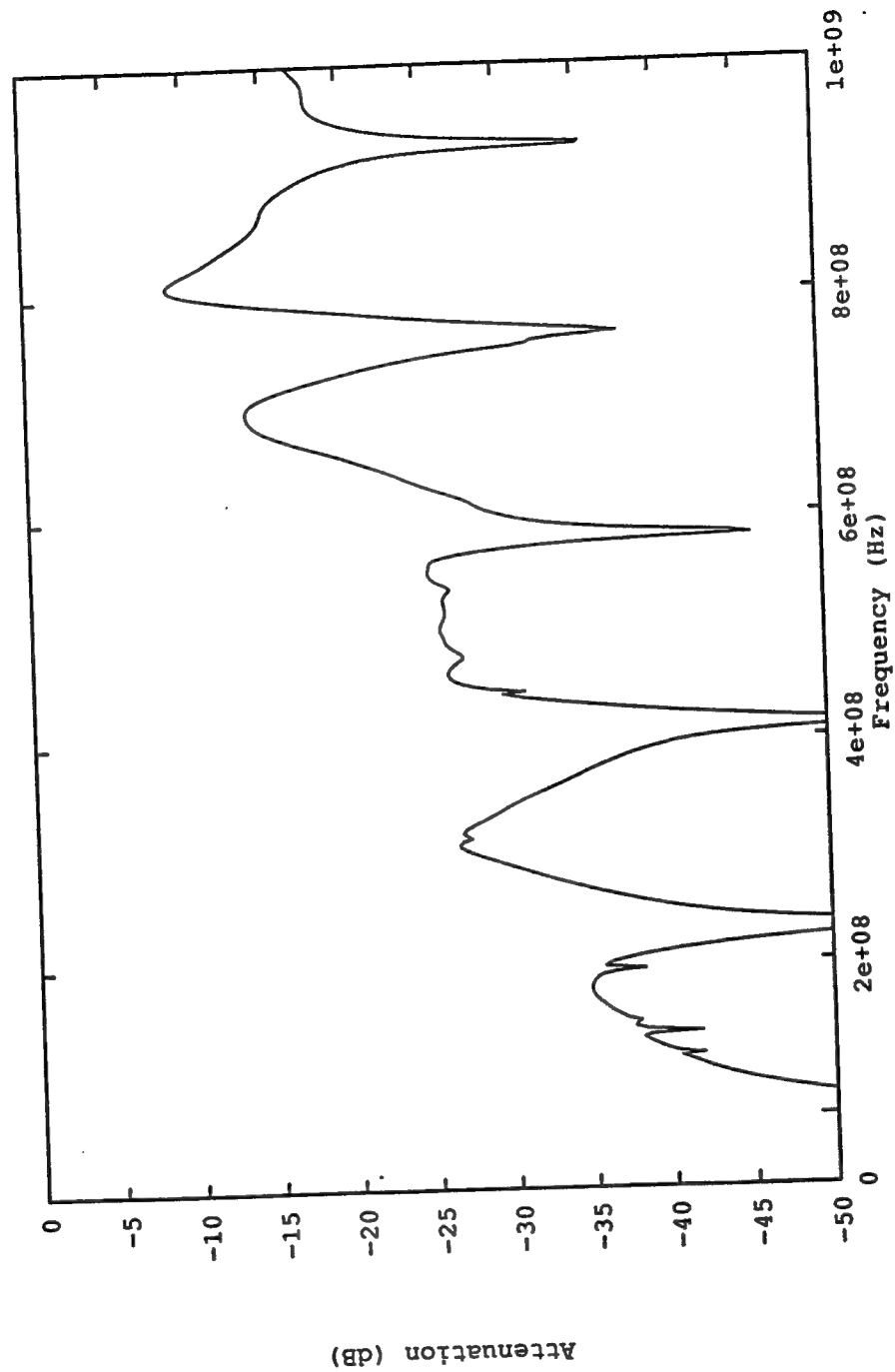
Figure 17. Tip Sensor S_{21} Magnitude.
7.23 cm Width Center Conductor, 1 cm AK Gap

39
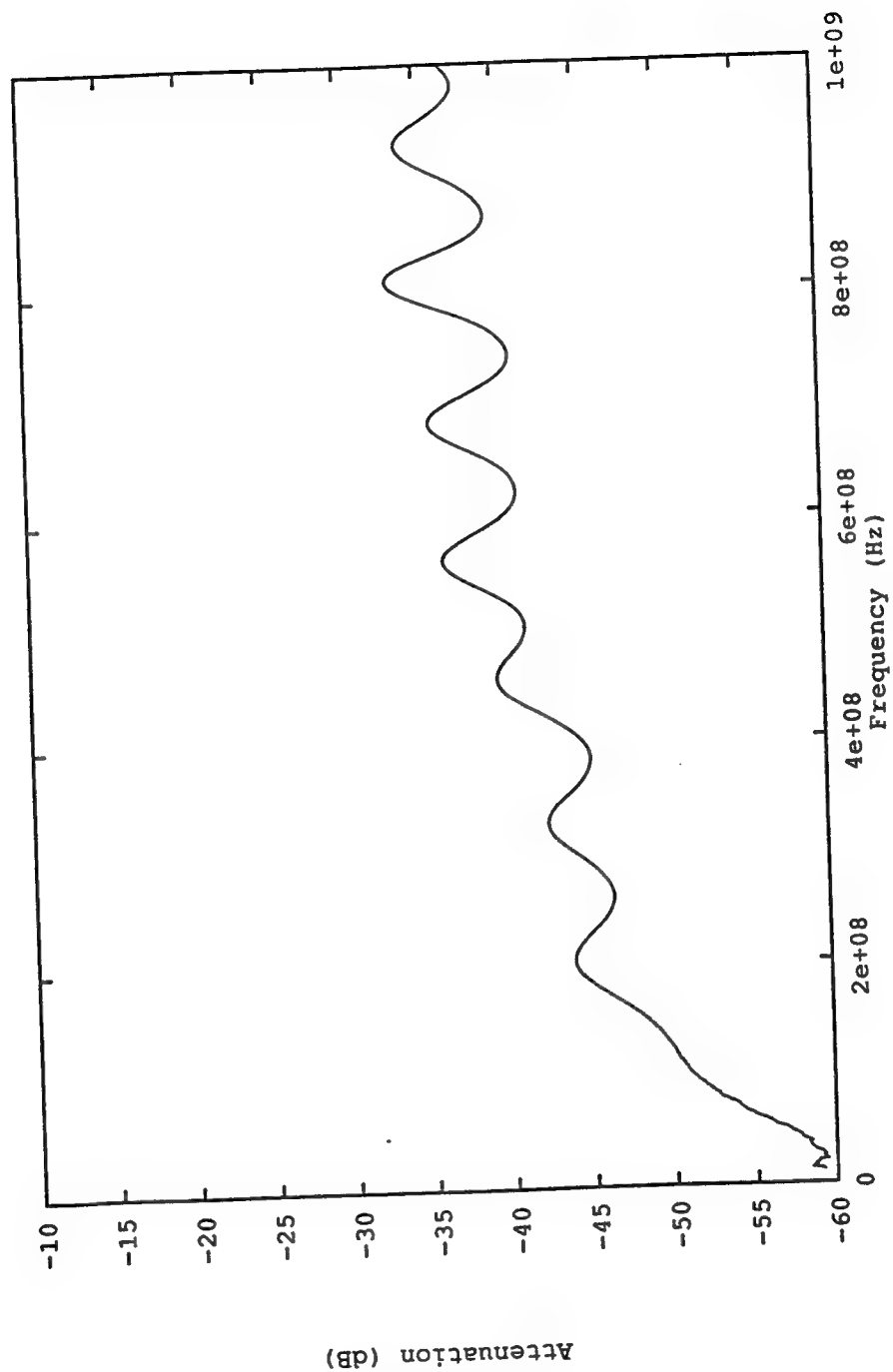
Figure 18. Tip Sensor S_{21} Magnitude.

1 cm Width Center Conductor, 0.14 cm AK Gap

40

The attenuation characteristics of the fiber optic cables are shown in figure 19 on page 42, a plot of attenuation versus wavelength. The abscissa is wavelength in nanometers while the ordinate is attenuation in decibels.

The spectrograph of the OMA was a Jarrell-Ash MonoSpec 27 Spectrograph with an entrance slit of 25 μ, and a grating of 150 g/mm blaze. The output of the Spectrograph was detected by an E.G.&G. Model 1254 SIT CCD.

The sensitivity curve of the CCD is shown in figure 20 on page 43, a plot of sensitivity versus wavelength. The abscissa is wavelength in nanometers while the ordinate is sensitivity in counts per photon.

The CCD was controlled by an E.G.&G. Model 1216 Multichannel Detector Controller and was triggered by and E.G.&G. Model 1211 High Voltage Pulse Generator.
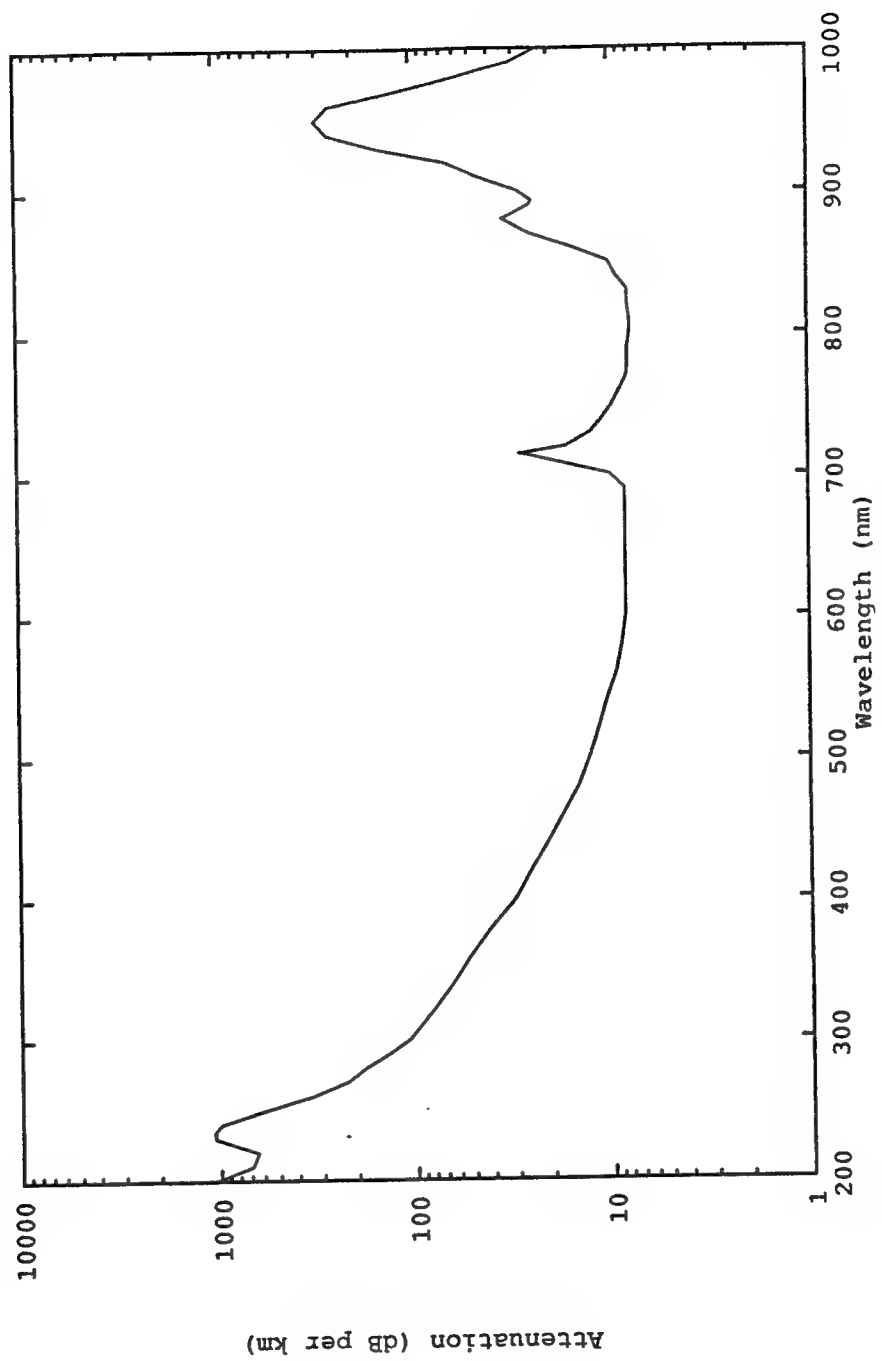
Figure 19. Fiber Optic Cable Attenuation

42
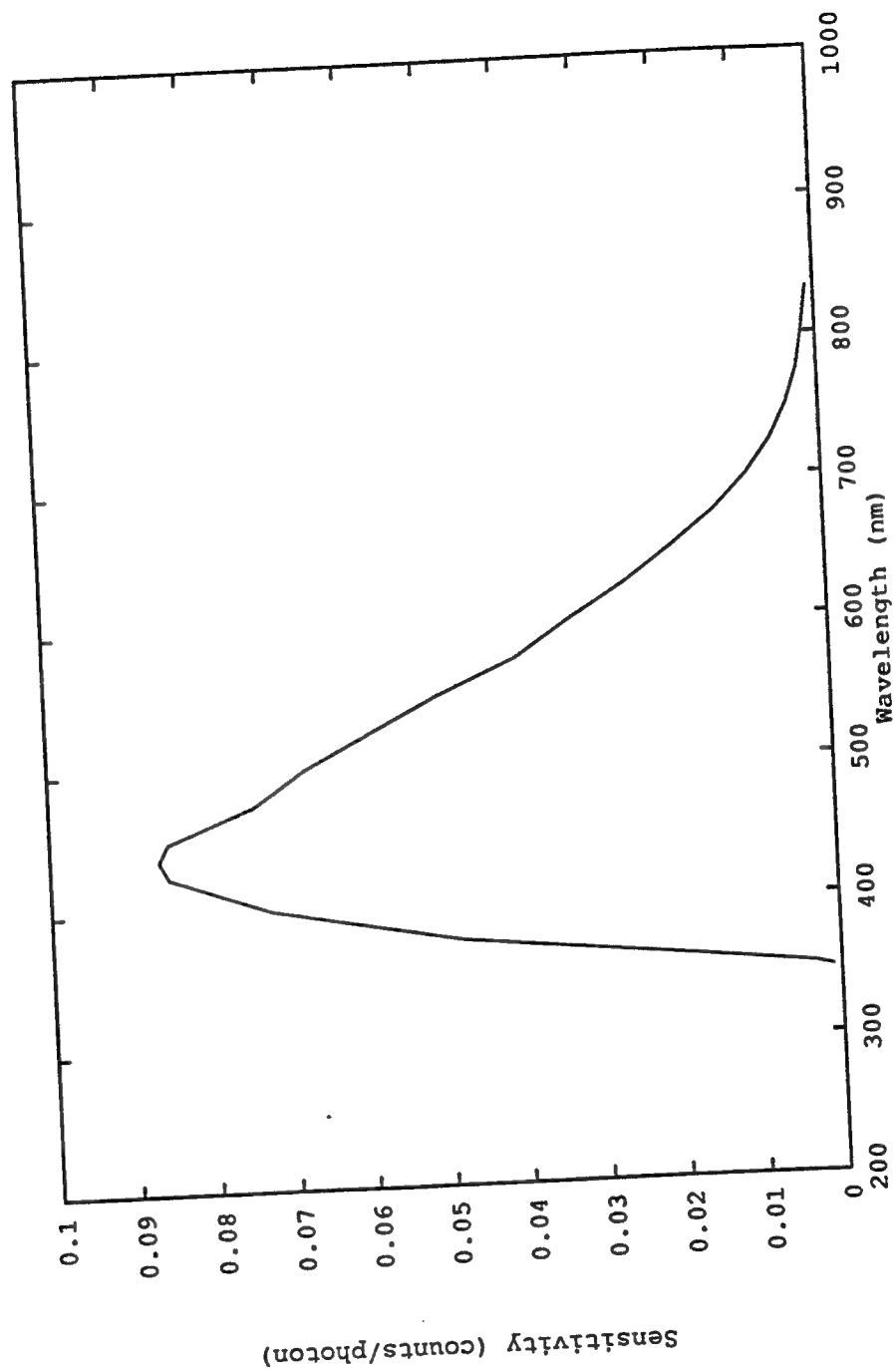
Figure 20. E.E.&G. Model 1254 SIT CCD Sensitivity

III B. EXPERIMENTAL PROCEDURE

The experimental procedure utilized the pulser's natural pulse length of 1.375 ns FWHM. The charge voltage was set at 18 kV yielding a peak signal of approximately 320 kV on the 50 Ω coaxial transmission line leading to the test chamber. Upon reflection of the pulse at the open circuit termination of the 50 Ω parallel plate transmission line, the voltage of the pulse doubles to 640 kV across a 1 cm gap. No seed ionization was employed in this experiment.

Table 1 shows the pressure, number of shots, and number of shots yielded by the experimental procedure. The annotation in the table of an evacuation indicates that the test chamber was evacuated to approximately 100 mTorr and then backfilled with dry nitrogen to the desired pressure. The test chamber was reconfigured with the narrow center conductor and the AK gap adjusted to 0.14 cm to provide a 50 Ω parallel plate transmission line for the 0.336 Torr shots. The number of shots yielded indicates the number of shots in which an arc has been detected. The procedure for detecting an arc is discussed in the next section, Data Reduction.

Pressure (Torr)	# Shots	Yield	Charge (kV)
Evacuated			18*
0.930	35	11	
Evacuated			18
685	12	10	18
295	14	10	18
150	10	10	18
73	12	10	18
29.5	11	10	18
19.5	22	7	18
1.07	13	5	18
0.506	19	5	20.125
0.506	21	7	
Evacuated			18
2.08	15	9	18
1.22	11	6	18
1.01	10	6	18
0.890	10	6	18
0.790	12	3	18
0.700	13	10	18
0.590	12	8	18
Evacuated			18
3.4	33	18	18
4.8	23	5	18
7.0	33	7	
Evacuated			20
0.336	44	24	

Table 1. Pressure versus Number of Shots

685 Torr to 0.336 Torr

* Transformer rebuild after this shot sequence

III C. DATA REDUCTION

The data was acquired as described in the experimental procedures section. The data was stored by the DCS01 software in log files which allowed the DCS01 software to maintain large amounts of data on files of no greater than 2200 bytes. These files had to be converted to ASCII files by a DCS01 software utility before data analysis could begin. After conversion to ASCII the data files were uploaded to a Sun SparcStation for analysis. The proper time base was added to the data files, and then the oscilloscope traces contained within the data files were transformed into frequency domain via a discrete Fourier transform so that corrections for cable and probe attenuation could be made. The oscilloscope trace data was then discrete inverse Fourier transformed back into the time domain, plotted, and examined for data quality. Data from shots in which the pulse power device did not perform properly, and data in which the oscilloscopes did not trigger properly, were eliminated from the data set.

Circuit modelling software had been used to estimate the rising and falling voltage slew rates to be expected for a circuit of this nature. Data which did not exhibit falling voltage slew rates in the neighborhood of these estimates were eliminated from the data set since a falling slew rate of

insufficient magnitude indicated that a discharge had not occurred.

The problem of establishing the beginning of the pulse had to be addressed. For the purposes of this investigation the beginning of the pulse was defined to occur when the electromagnetic field exceeds the dc breakdown value of 15.54 V/cm/Torr. This definition is due to the pulse width of the applied electromagnetic field, since the conditions necessary for dc breakdown are never achieved.

The theory upon which this investigation is based assumes that a triangular shaped pulse excites the nitrogen to breakdown (refer to appendix B). Data which exhibited waveforms other than triangular in nature were eliminated from the data set. For this purpose the criteria used required that no localized minima exist between the beginning of the pulse and the point at which breakdown occurred. The resulting data yield after elimination of suspect shots was approximately 48.6 percent.

Two channels of optical data were acquired to provide a verification of the N_2 spectrum produced by arcing. A cable 25 m long viewed the discharge perpendicular to the arc while a cable 50 m long viewed the discharge down the axis of the arc. The optical data was acquired by the E.E.&G. O.M.A. and

47

stored to data files in a format peculiar to the O.M.A. The data files were converted to ASCII by a software program developed at the Phillips Laboratory, and then uploaded to a Sun SparcStation. The data was adjusted for fiber optic cable attenuation and geometrical effects of probe placement, and then plotted and examined for the characteristics of the N_2 spectrum. The data was not adjusted for CCD sensitivity since the effects of the sensitivity were equal in both optical data channels.

III D. DATA ANALYSIS

The data which was acquired as described in the experimental procedures section is presented in figure 21 on page 50, a plot of E_o/P versus $P\tau_p$. The ordinate represents E_o/P in V/cm/Torr while the abscissa represents $P\tau_p$ in Torr-s. The solid line is the theoretical relativistic estimate of Graham and Roussel-Dupré, while the dashed line is the classical estimate as discussed in the classical theory section. The symbols represent the breakdown points acquired during the course of experiment which survived the data reduction process.

The data from each pressure setting except for 0.336 Torr to 0.790 Torr, and 0.930 Torr was averaged to obtain mean values and standard deviations for E_o/P and $P\tau_p$. Only the $P\tau_p$ values obtained for 0.336 Torr to 0.790 Torr, and 0.930 Torr were averaged. The E_o/P values obtained for 0.336 Torr to 0.790 Torr, and 0.930 Torr were not averaged as the data at this pressure establishes the lower limit of $P\tau_p$ under the prevailing experimental conditions.
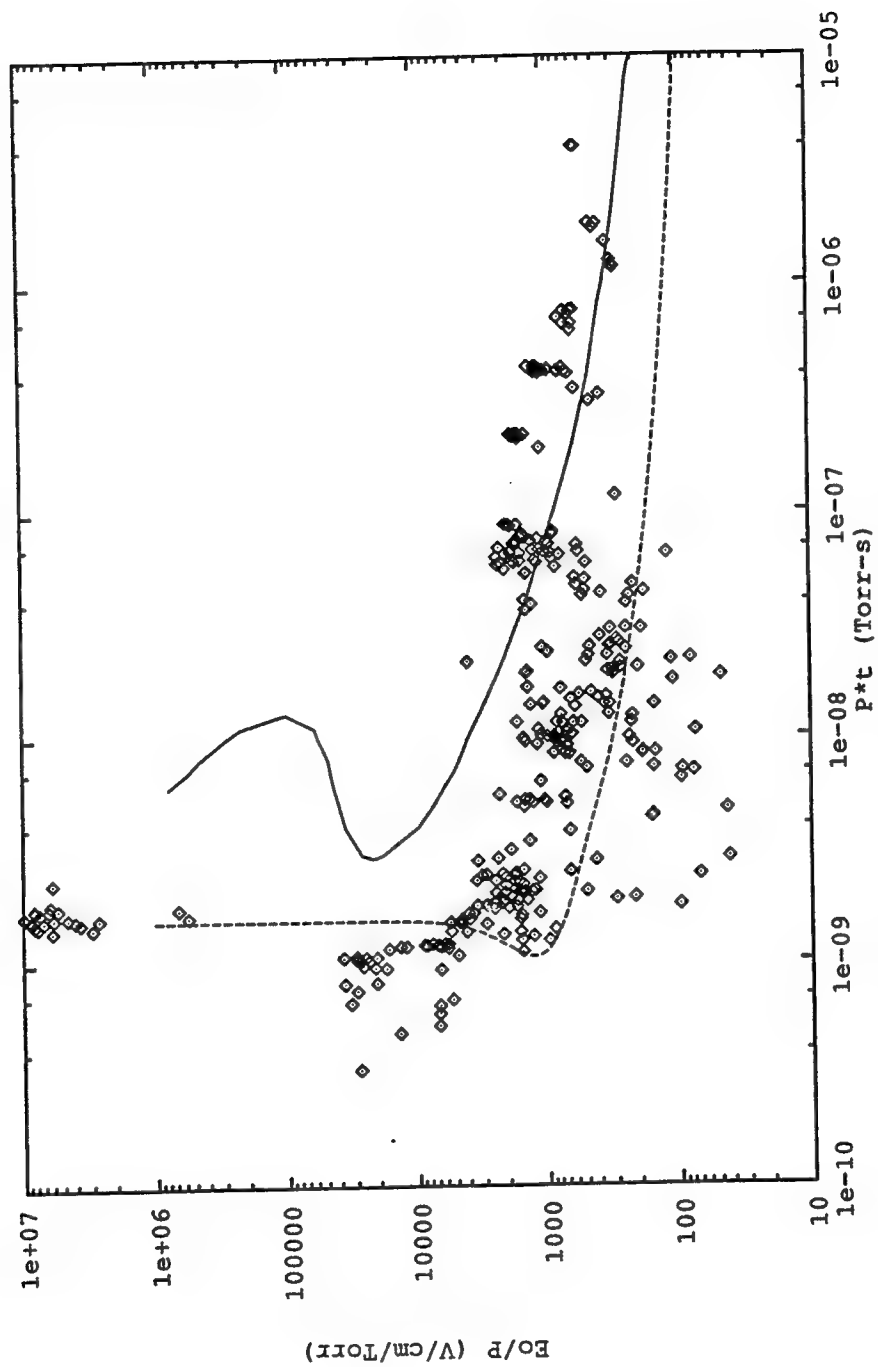
Figure 21. E_o/P vs. $P\tau_p$ Data Compared to

Classical and Relativistic Theory

The mean values of E_o/P and $P\tau_p$ with their standard deviations shown in brackets are presented below in table 2 for each operational test pressure.

Press. (Torr)	Mean E_o/P (V/cm/Torr)	Mean $P\tau_p$ (Torr-s)
685	0.337×10^3 (0.060×10^3)	0.145×10^{-5} (0.030×10^{-5})
295	0.638×10^3 (0.056×10^3)	0.706×10^{-6} (0.048×10^{-6})
150	0.112×10^4 (0.007×10^4)	0.421×10^{-6} (0.009×10^{-6})
73	0.160×10^4 (0.011×10^4)	0.216×10^{-6} (0.003×10^{-6})
29.5	0.165×10^4 (0.018×10^4)	0.794×10^{-7} (0.065×10^{-7})
19.5	0.162×10^4 (0.037×10^4)	0.589×10^{-7} (0.046×10^{-7})
7.0	0.304×10^3 (0.028×10^4)	0.211×10^{-7} (0.023×10^{-7})
4.8	0.623×10^3 (0.100×10^3)	0.134×10^{-7} (0.025×10^{-7})
3.4	0.923×10^3 (0.313×10^3)	0.983×10^{-8} (0.086×10^{-8})
2.08	0.135×10^4 (0.045×10^4)	0.516×10^{-8} (0.018×10^{-8})
1.22	0.201×10^4 (0.072×10^4)	0.286×10^{-8} (0.040×10^{-8})
1.07	0.228×10^4 (0.063×10^4)	0.239×10^{-8} (0.012×10^{-8})
1.01	0.189×10^4 (0.072×10^4)	0.200×10^{-8} (0.040×10^{-8})
0.890	0.165×10^4 (0.039×10^4)	0.207×10^{-8} (0.023×10^{-8})
0.790		0.200×10^{-8} (0.007×10^{-8})
0.700		0.176×10^{-8} (0.010×10^{-8})
0.590		0.150×10^{-8} (0.008×10^{-8})
0.506 (18kV)		0.119×10^{-8} (0.008×10^{-8})
0.506 (20.125kV)		0.118×10^{-8} (0.002×10^{-8})
0.336		0.162×10^{-8} (0.012×10^{-8})
0.930 (Transformer Rebuild)		0.102×10^{-8} (0.006×10^{-8})

Table 2.   Mean E_o/P and $P\tau_p$.

Data which did not lie within ± 3 standard deviations of the mean values was regarded as suspect and eliminated from the population. The data which remained is presented in figure 22 on page 52, a plot of E_o/P versus $P\tau_p$. The ordinate represents E_o/P in V/cm/Torr, the abscissa represents $P\tau_p$ in Torr-s. The solid line represents the estimate of Graham and Roussel-Dupré, while the dashed line is the classical estimate.
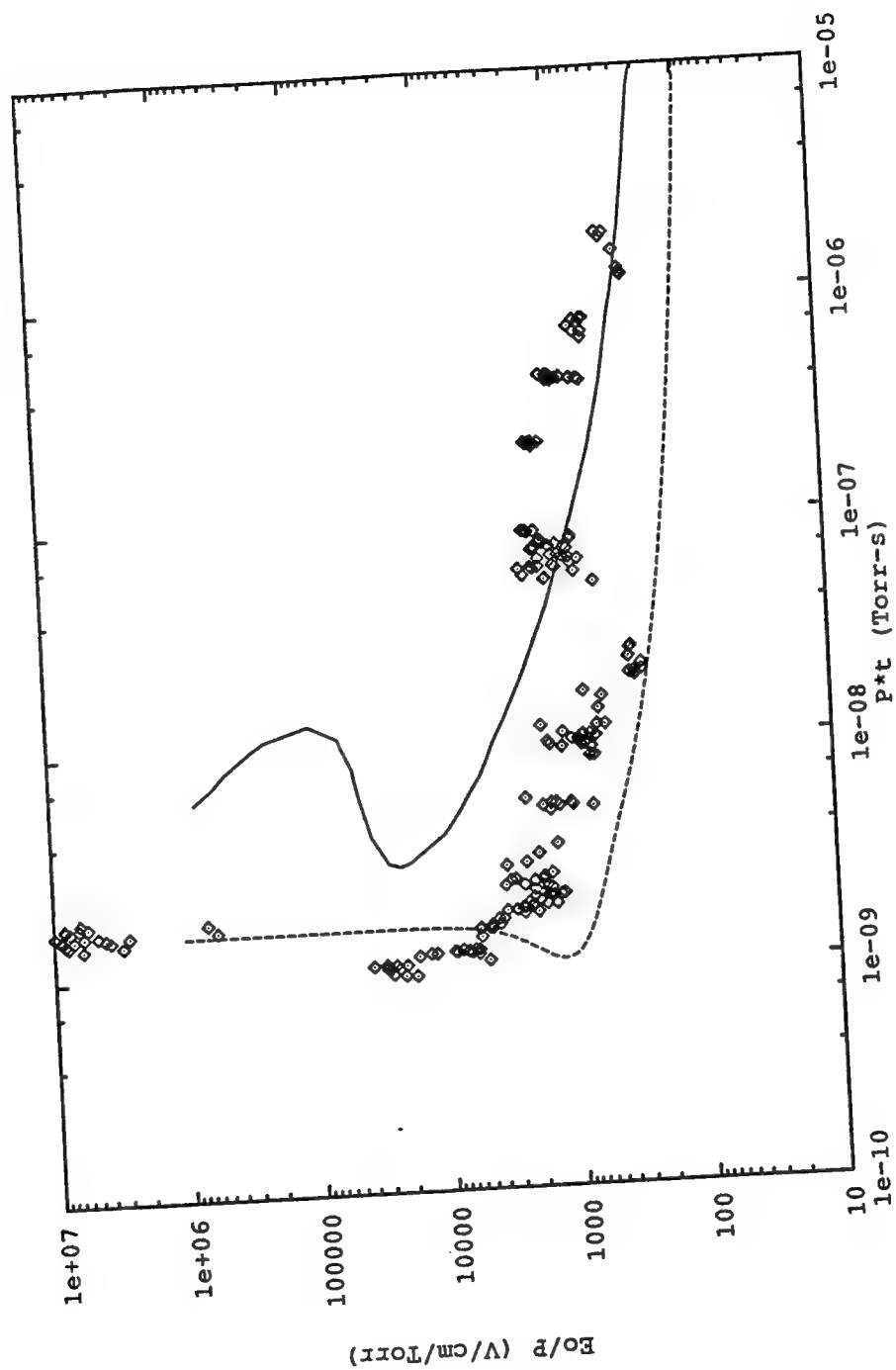
Figure 22. Edited E_0/P vs. $P\tau_p$ Data
Compared to Classical and Relativistic Theory

The mean values, with error bars representing ±1.5 standard deviations, and the edited 0.336 Torr to 0.790 Torr, and 0.930 Torr data are presented in figure 23 on page 54, a plot of E_o/P versus $P\tau_p$. The ordinate represents E_o/P in V/cm/Torr while the abscissa represents $P\tau_p$ in Torr-s. As in figure 22, the solid line is the relativistic estimate while the dashed line is the classical estimate. The symbols represent the mean breakdown points or edited data, calculated as described above.

The discontinuity in the region of approximately 3×10^{-9} Torr-s to 4×10^{-8} Torr-s is suspected to be due to multichanneling of the discharge. It has been observed in the WFX experiment[33] that at approximately 30 to 40 Torr arcing phenomenon transitions from single channel arcing through multichannel arcing to a symmetric aural discharge, and then transitions back to single channel arcing at approximately 3 to 4 Torr. The WFX experiment was an investigation of the utilization of hydrogen gas as a working fluid for the production of plasma, with the multichanneling effect behaving as a smooth transition from 40 Torr to 4 Torr.
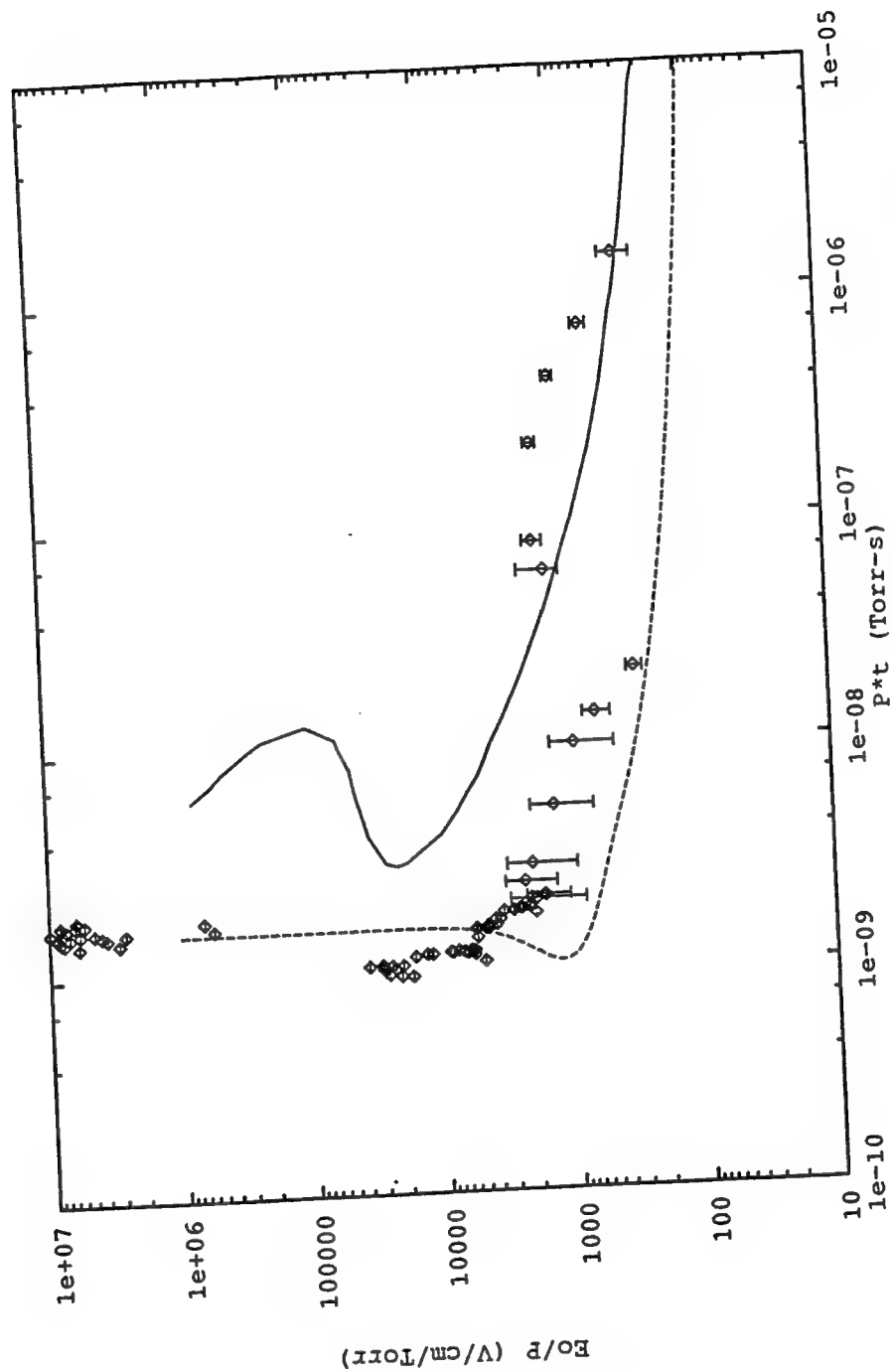
Figure 23. Mean and Edited E_o/P vs. $P\tau_p$ Values Compared to Classical and Relativistic Theory

The multichanneling effect would be physically limited by the number channels available. The arc diameter of this experiment as measured from polaroid photographs of single arcing events indicates a maximum of 0.5 cm per channel. The width of electrode available for arcing is 7.23 cm, which allows approximately 14 simultaneous channels. Assuming that each channel has the same resistance yields an equivalent resistance for an aura discharge which is one fourteenth that of the single channel resistance. This is illustrated in figure 24 (A) and (B). Note that V_{mc}, the multichanneling voltage, is the square root of one-fourteenth V.

$$V = IR$$

(A)

$$V_{mc} = I_{mc}R_{eq} = IR/\sqrt{14}$$

(B)
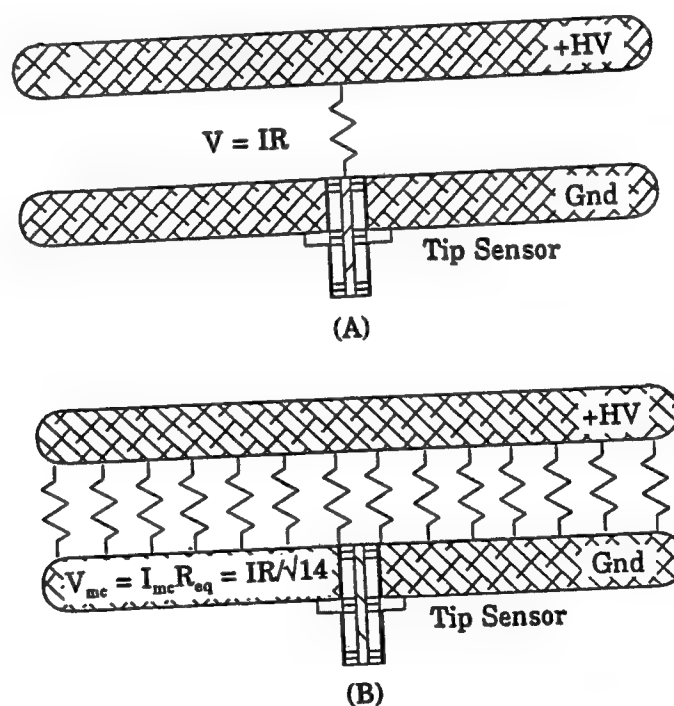
Figure 24. Multichanneling Geometries

55

For a one ns RF pulse this would indicate a transition region on the paschen curve from approximately 3×10^{-9} Torr-s to approximately 4×10^{-8} Torr-s. A transition region such as this is supported by the experimental data, which shows a drop in the E_o/P values in the transition region by roughly one order of magnitude.

The data was corrected for the multichanneling effect by graphically selecting an E_o/P value, and the corresponding $P\tau_p$ value, of greatest magnitude above 4×10^{-8} Torr-s and graphically selecting the most comparable E_o/P value, and the corresponding $P\tau_p$ value, below 4×10^{-8} Torr-s. The lowest value of E_o/P, and the corresponding $P\tau_p$ value, in between these two boundary values was assumed to approximately be the location of the symmetrical aural discharge. These assumptions were made due to the uncertainities introduced because of the difference in the working fluids of each experiment, hydrogen and nitrogen. The $P\tau_p$ values selected for the upper and lower bounds were 7.94×10^{-8} Torr-s and 2.39×10^{-9} Torr-s respectively. The symmetrical aura was assumed to occur at 2.11×10^{-8} Torr-s. A straight line was visually fit to the data lying between the aural discharge and the lower bound via a log-log graph. The data was then adjust by a logarithmic amount to compensate for the multichannelling effect. $\sqrt{18}$ was selected as the maximum scaling factor since a symmetrical aura could support a

minimum of the equivalent of 18 simultaneous channels.
Likewise, a straight line was visually fit to the data lying
between the aural discharge and the upper bound via a log-log
graph. The data was then adjust by a logarithmic amount to
compensate for the multichannelling effect again scaling the
result to yield a value of $\sqrt{18}$ at 2.11×10^{-8} Torr-s.

The E_o/P values and their standard deviations were rescaled
yielding a Paschen curve as shown in figure 25 on page 59, a
plot of E_o/P versus $P\tau_p$. The ordinate represents E_o/P in
V/cm/Torr while the abscissa represents $P\tau_p$ in Torr-s. The
solid line is the theoretical relativistic estimate of Graham
and Roussel-Dupré, while the dashed line is the classical
estimate as discussed in the classical theory section. The
symbols represent the breakdown points corrected for
multichanneling.

Having corrected for the multichannel effects the data
conforms most precisely to the classical theory developed in
this investigation, with the exception of a shift in the
magnitude of E_o/P. This shift in magnitude is indicative of
an incorrect value for v_{eff}. Estimation of an appropriate v_{eff}
yields a value which is approximately 6 times that classically
assumed. The classical theory developed in this investigation
was adjusted to account for the greater value for v_{eff} and

57

recomputed. The results of this reevaluation are shown in figure 26 on page 60, a plot of E_o/P versus $P\tau_p$. The ordinate represents E_o/P in V/cm/Torr while the abscissa represents $P\tau_p$ in Torr-s. The solid line is the theoretical relativistic estimate of Graham and Roussel-Dupré, the long dashed line is the classical estimate as discussed in the classical theory section, while the short dashed line is the classical estimate corrected ν_{eff}. The symbols represent the breakdown points corrected for multichanneling.
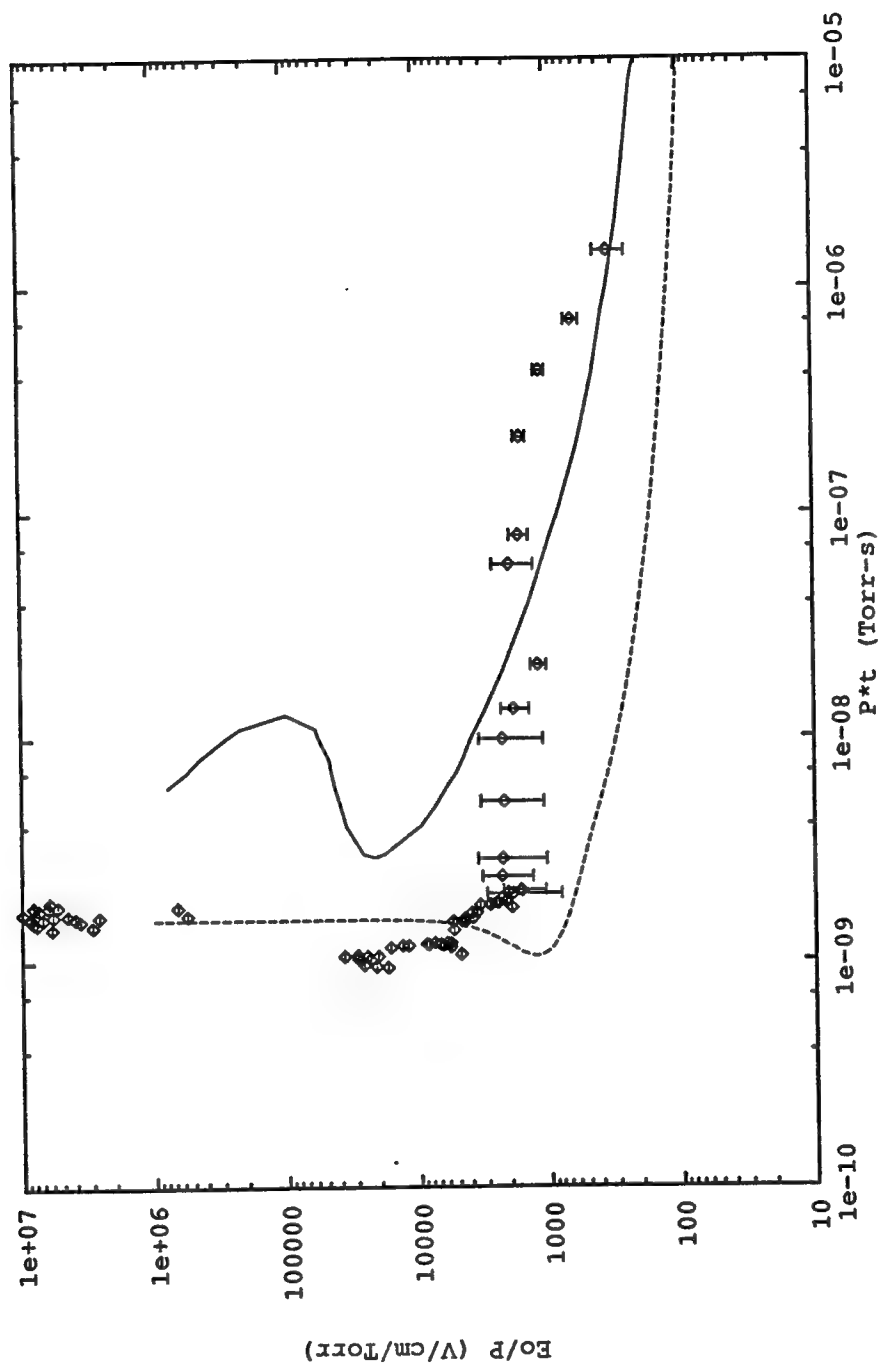
Figure 25. Corrected E_o/P vs. $P\tau_p$ Values

Compared to Classical and Relativistic Theory
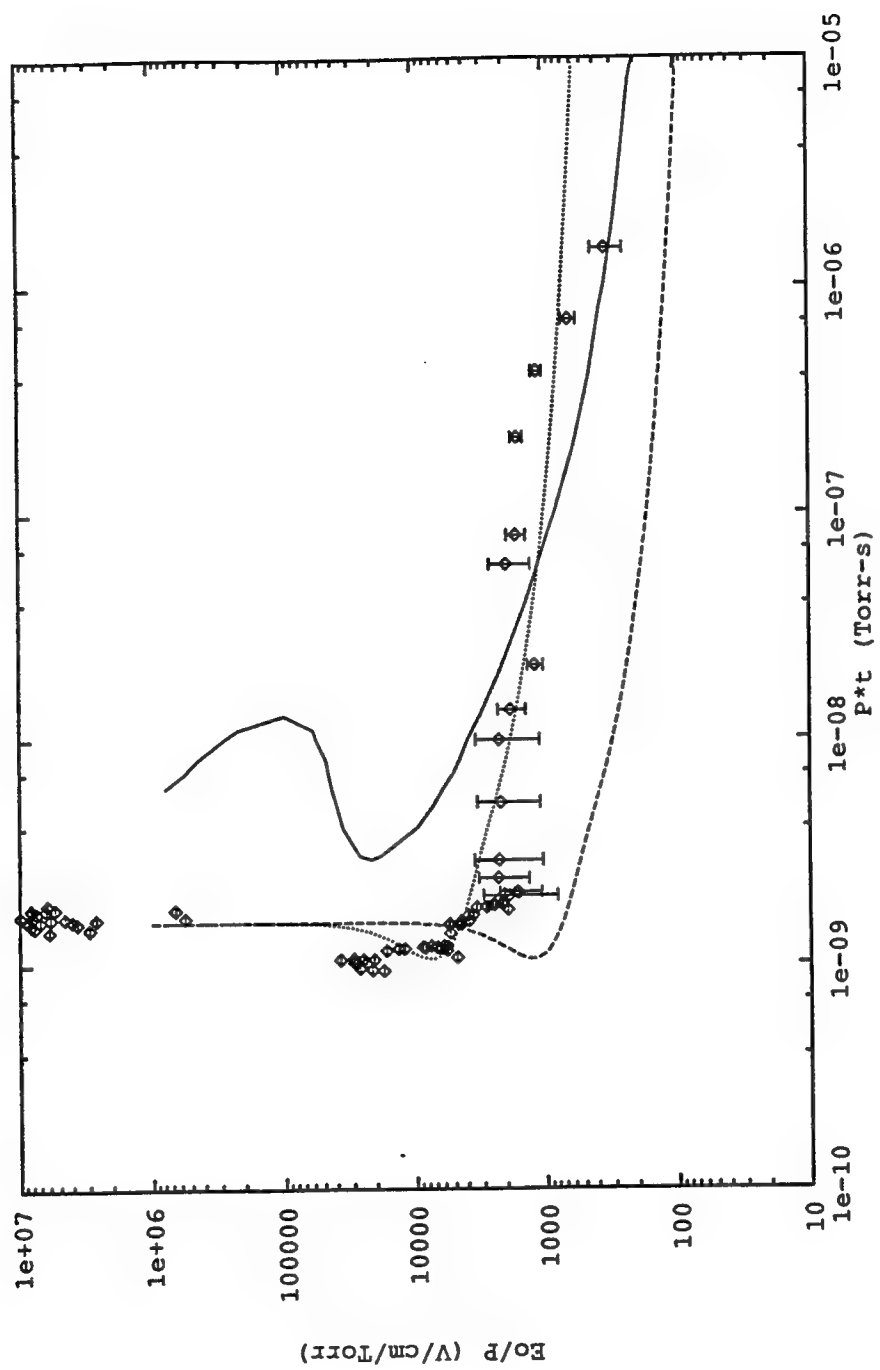
Figure 26. Corrected E_o/P vs. $P\tau_p$
Compared to Corrected Classical Theory

A tabulation of the mean pulse length to breakdown at each pressure is presented in table 3. Also presented is the number of points which constitute the mean. The overall mean pulse length to breakdown was 2.373 ns.

Pressure in Torr	τ_p in ns	# of pts.
0.930	1.103	11
685	2.117	10
295	2.393	10
150	2.807	10
73	2.959	10
29.5	2.692	10
19.5	3.201	7
7.0	3.014	7
4.8	2.792	5
3.4	2.891	18
2.08	2.481	9
1.22	2.344	6
1.07	2.234	5
1.01	1.980	6
0.890	2.326	6
0.790	2.532	3
0.700	2.513	10
0.590	2.551	8
0.506	2.304	5
0.506	2.332	7
0.336	1.638	24

Table 3. Breakdown Pulse Length

Comparing the experimentally obtained spectra acquired by the spectrograph during a discharge to the spectra for nitrogen from the CRC Handbook suggests that the light pulse produced by the electrical discharge is due to electron energy transitions in nitrogen. No aluminum lines were evident in the spectra.

A discrete Fourier transform was perform on the data to compensate for the attenuation of the cables and probes. A typical Fourier transform of an electrical discharge is shown in figure 27 on page 63, a plot of frequency versus amplitude after compensation for cable and probe attenuation. The ordinate represents frequency in Hz while the abscissa represents amplitude in V/Hz. The localized maxima in figure 27 represent the maximum probe attenuation at those frequencies, refer to figure 17. The overall peak frequency component - neglecting the localized maxima - occurs at approximately 100 to 200 MHz.

The previous efforts utilized predominately monofrequency sources. The results of Felsenthal and Proud were obtained for a pulsed D.C. experimental system, and the results of Ali and Coffey were calculated for 10 GHz and 3 GHz. Thus the broadband signal should be bounded on the bottom by the work of Felsenthal and Proud, and on the top by the results of Ali and Coffey. This is graphically presented in figure 28 on page 64, a plot of E_o/P versus $P\tau_p$. The ordinate represents E_o/P in V/cm/Torr while the abscissa represents $P\tau_p$ in Torr-s. The boundary limits apply between approximately 4×10^{-9} Torr-s to 5×10^{-7} Torr-s, where departures from the limiting values occur. These departures are attributed to the broadband nature of this investigation.
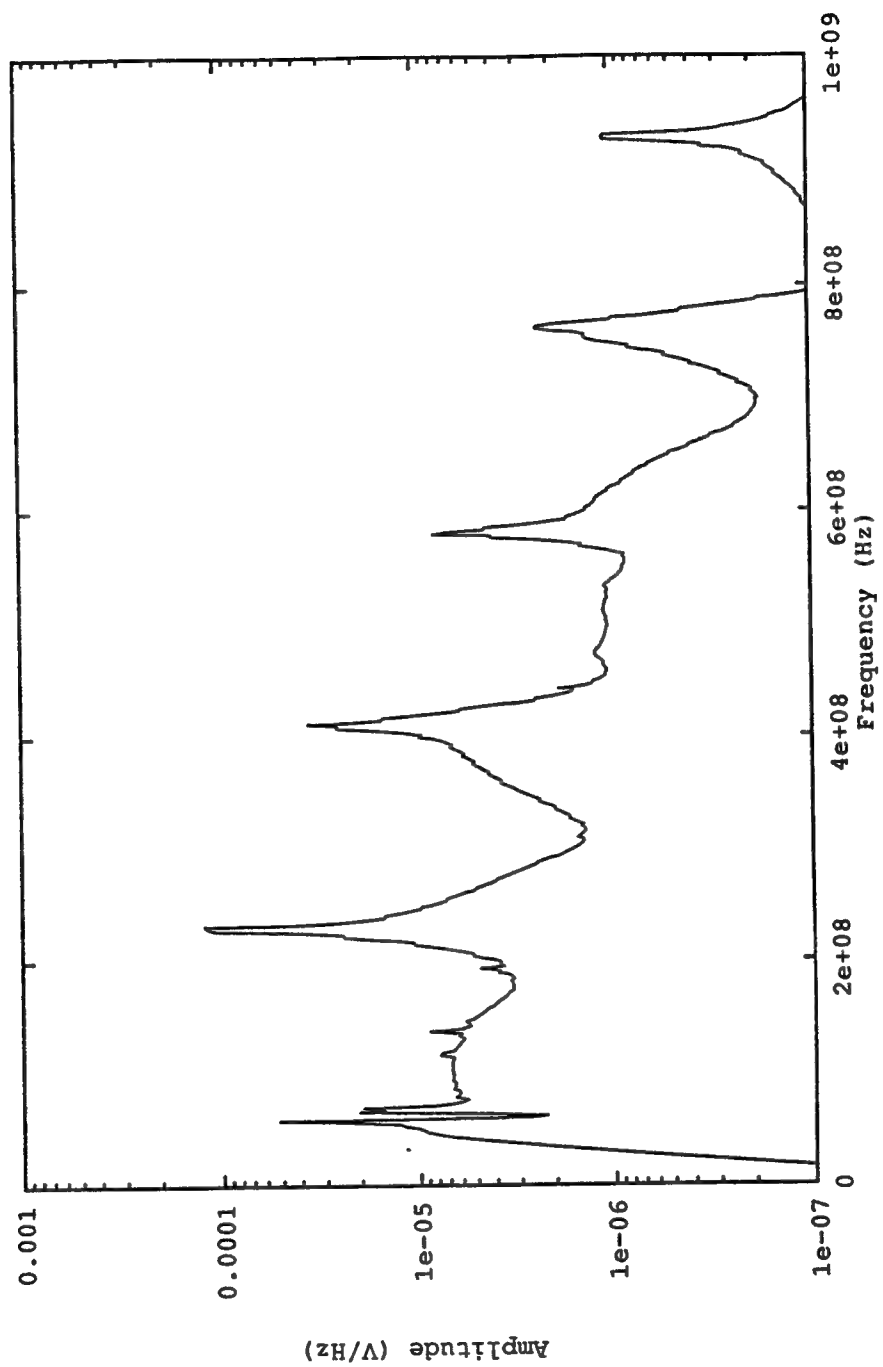
Figure 27. Amplitude vs. Frequency

Discrete Fourier Transform of N_2 Discharge

63
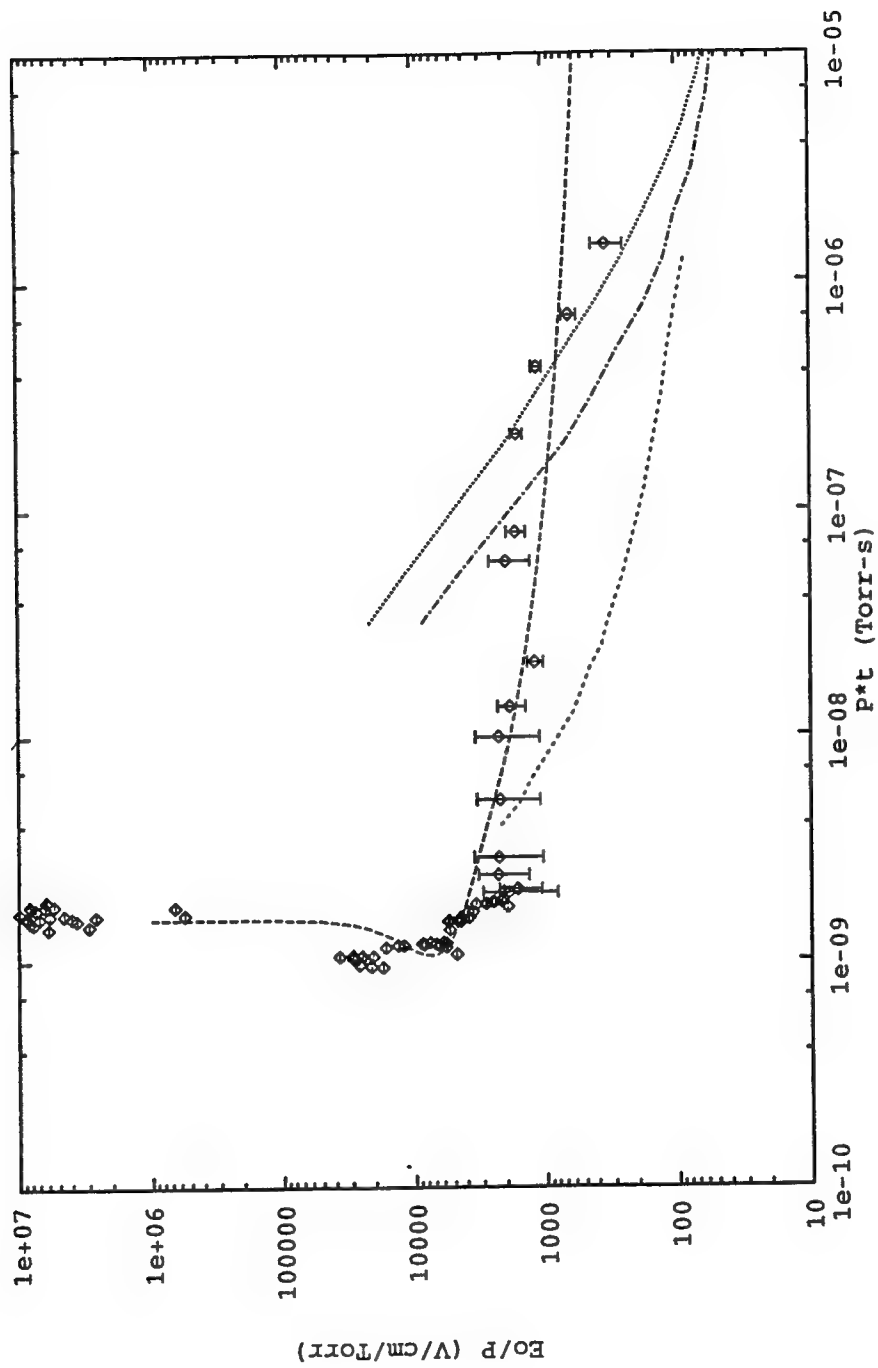
Figure 28. Corrected E_o/P vs. $P\tau_p$

Corrected Classical Theory Compared to Prior Investigations

64

CONCLUSIONS

The data suggests that multichanneling occurs between 2.39×10^{-9} Torr-s and 7.94×10^{-8} Torr-s. This implies that gaseous switch design may be modified to take advantage of the multichanneling effect to produce switches which close at a lower E_o/P value by allowing for multiple channels or symmetric aura. This further implies that gaseous switch design may be modified to take advantage of the multichanneling effect to produce switches which can close at selectable E_o/P values for a set $P\tau_p$ value.

The data corrected for multichanneling suggests that the ν_{eff} assumed for classical monofrequency Paschen curve investigations underestimates the ν_{eff} for broadband Paschen curve investigations by a factor of approximately 6. This would imply that the ν_{eff} is frequency dependent.

The reversal feature of the Paschen curve has not been observed in the experimental results. The relativistic Paschen curve of Graham and Roussel-Dupré may not have been noted below 4×10^{-8} Torr-s for the following reasons:

The relativistic theory has been developed to describe phenomena in the upper atmosphere. This

65

implies a theory based on fixed pressure and variable pulse length. The experimental data acquired in this investigation is based on variable pressure and fixed pulse length. It has been proposed[32] that the divergence from the relativistic theory to the classical theory at approximately 4×10^{-8} Torr-s could be a transition region from fixed pressure and variable pulse length physics to variable pressure and fixed pulse length physics.

The relativistic theory of Graham and Roussel-Dupré naturally requires that the electrons achieve relativistic velocities. This issue been examined in the context of this investigation[35]. A velocity estimate had been obtained by dividing the acceleration of a free electron in a 1×10^7 V/m field by the classical estimate for V_{eff} at 1 Torr, yielding a β of approximately 1. To calculate the collisional velocity of this investigation requires a knowledge of the mean free path length[32].

$$\overline{\lambda} = \frac{1}{N_{N_2} \pi \lambda_d^2} \qquad (25)$$

where: λ_d = debye length

N_{N2} = Density of nitrogen

Referring to equation C-25 it is recalled that

$$\lambda_d = \sqrt{\frac{\varepsilon_o R_o T}{23.8 \times 10^8 PQ}} \sqrt{\frac{E}{Q}} \qquad (26)$$

Using the classical physics equation $x = \frac{1}{2}at^2$, recalling the Lorentz force equation $m_e a = qE_{field}$ to calculate acceleration, and setting x equal to the mean free path length yields an equation for the mean collisional time, t_{coll}. Numerically solving for t_{coll}, and then calculating the electron velocity at the time of collision yields an estimated maximum electron velocity of $\beta = 1.7 \times 10^{-6}$. This is insufficient for the observation of relativistic effects.

The theory of Graham and Roussel-Dupré has been developed assuming intense E-fields, B-fields, and propagation vectors. The experimental setup of

this investigation reflected an RF pulse off of an open transmission line, effectively canceling the incident B-field and propagation vector with the reflected B-field and propagation vector, see figure 29. The relativistic fluid equations[23] collapse to classical equations under these conditions. For relativistic effects to be observed requires either a B-field or electron flow in the direction of the propagation vector.
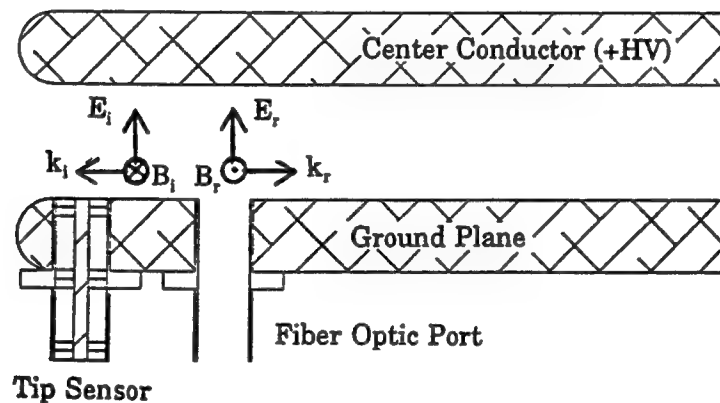
Figure 29. Field Geometries at Tip

Classical theory and experimental data suggest that a collisional frequency limit of approximately 1×10^{-9} Torr-s exists. This implies that an intense electrical pulse may be created in a gaseous medium without breakdown occurring if the parameter of pulse length multiplied by pressure does not exceed 1×10^{-9} Torr-s.

APPENDIX A

Evaluation of the Ionization Rate

Integrals

Evaluation of integral 11 as listed in the main text

$$\langle\frac{v_i}{P}\rangle = 6x10^7\sqrt{\frac{27}{2\pi}}\,\varepsilon^{-3/2}\,[\alpha\int_{E_i}^{400}E(E-E_i)\exp\{\frac{E_i-E}{\beta}\}\exp\{\frac{-3E}{2\varepsilon}\}dE +$$

$$10^2\int_{400}^{\infty}\sqrt{E}\exp\{\frac{-3E}{2\varepsilon}\}dE] \qquad\qquad \textbf{A-1}$$

may be performed in the following manner.

$$\langle\frac{v_i}{P}\rangle = 6x10^7\sqrt{\frac{27}{2\pi}}\,\varepsilon^{-3/2}\,[\alpha\exp\{\frac{E_i}{\beta}\}\int_{E_i}^{400}E^2\exp\{-[\frac{1}{\beta}+\frac{3}{2\varepsilon}]E\}dE -$$

$$\alpha E_i\exp\{\frac{E_i}{\beta}\}\int_{E_i}^{400}E\exp\{-[\frac{1}{\beta}+\frac{3}{2\varepsilon}]E\}dE +$$

$$10^2\int_{400}^{\infty}\sqrt{E}\exp\{\frac{-3E}{2\varepsilon}\}dE] \qquad\qquad \textbf{A-2}$$

Evaluate each integral separately. The strategy to be used will begin with the evaluation of the second integral in equation A-2, continue with the first integral, and conclude with the evaluation of the last integral.

70

First evaluate the second integral in equation A-2. Begin by defining $k_o = 1/\beta + 3/2\varepsilon = [2\varepsilon+3\beta]/(2\beta\varepsilon)$.

$$\int_{E_1}^{400} E\exp(-k_o E)dE = \frac{-\partial}{\partial k_o} \int_{E_1}^{400} \exp(-k_o E)\, dE \qquad \textbf{A-3}$$

$$-\frac{\partial}{\partial k_o} \frac{\exp(-k_o E)}{k_o}\Big|_{E_1}^{400} = -\frac{\partial}{\partial k_o}\left[\frac{\exp(-400k_o)-\exp(-E_1 k_o)}{k_o}\right] \qquad \textbf{A-4}$$

Thus

$$\int_{E_1}^{400} E\exp(-k_o E)\, dE = -\left[\frac{\exp(-400k_o)-\exp(-E_1 k_o)}{k_o^2}\right]$$

$$+\left[\frac{-400\exp(-400k_o)+E_1\exp(-E_1 k_o)}{k_o}\right] \qquad \textbf{A-5}$$

However $E_i \ll 400$ eV and $1/k_o = 2\beta\varepsilon/[2\varepsilon+3\beta]$, therefore

71

$$\int_{E_1}^{400} E \exp\left(-k_o E\right) dE \approx \frac{\exp\left(-E_i k_o\right)}{k_o} \left[\frac{1}{k_o} + E_i\right] \qquad \textbf{A-6}$$

and

$$\int_{E_1}^{400} E \exp\left(-\left[\frac{1}{\beta} + \frac{3}{2\varepsilon}\right] E\right) dE =$$

$$\frac{2\beta\varepsilon}{2\varepsilon+3\beta} \left(\frac{2\beta\varepsilon}{2\varepsilon+3\beta} + E_i\right) \exp\left(\frac{-E_i}{\beta}\right) \exp\left(\frac{-3E_i}{2\varepsilon}\right) \qquad \textbf{A-7}$$

72

Evaluation of the first integral in equation A-2 is best accomplished by taking the partial with respect to k_o of the second integral in equation A-2. Thus, the partial with respect to k_o of equation A-6 will yield the solution.

$$\int_{E_1}^{\infty} E^2 \exp(-k_o E)\, dE = \frac{-\partial}{\partial k_o} \int_{E_1}^{400} E \exp(-k_o E)\, dE = \frac{-\partial}{\partial k_o} \frac{\exp(-E_1 k_o)}{k_o} \left[\frac{1}{k_o} + E_1\right]$$

$$= \frac{2\exp(-E_1 k_o)}{k_o^3} + \frac{2E_1 \exp(-E_1 k_o)}{k_o^2} + \frac{E_1^2 \exp(-E_1 k_o)}{k_o}$$

$$= \exp(-E_1 k_o) \left[\frac{2}{k_o^3} + \frac{2E_1}{k_o^2} + \frac{E_1^2}{k_o}\right]$$

Thus

$$\int_{E_1}^{400} E^2 \exp(-k_o E)\, dE = \frac{\exp(-E_1 k_o)}{k_o} \left[\frac{2}{k_o^2} + \frac{2E_1}{k_o} + E_1^2\right]$$

and finally

$$\int_{E_1}^{400} E^2 \exp\left(-\left[\frac{1}{\beta} + \frac{3}{2\varepsilon}\right] E\right) dE =$$

$$\frac{2\beta\varepsilon}{2\varepsilon + 3\beta} \left[\frac{8(\beta\varepsilon)^2}{(2\varepsilon + 3\beta)^2} + \frac{4\beta\varepsilon E_1}{2\varepsilon + 3\beta} + E_1^2\right] \exp\left(\frac{-E_1}{\beta}\right) \exp\left(\frac{-3E_1}{2\varepsilon}\right) \qquad \textbf{A-8}$$

73

Finally evaluate the third integral in equation A-2, with the definition of $k = 3/2\varepsilon$, and the substitution of $x = E^{1/2}$.

$$\int_{400}^{\infty} \sqrt{E}\exp\{\frac{-3E}{2\varepsilon}\}dE = \int_{20}^{\infty} x\exp(-kx^2)\,dx^2$$

$$-2\int_{20}^{\infty} x^2\exp(-kx^2)\,dx = -2\frac{\partial}{\partial k}\int_{20}^{\infty}\exp(-kx^2)\,dx = -2\frac{\partial}{\partial k}I$$

Now note that

$$I^2 = \int_{2020}^{\infty}\int \exp[-k(x^2+y^2)]\,dxdy = \int_{\sqrt{800}}^{\infty}\int_{0}^{2\pi} r\exp(-kr^2)\,drd\theta$$

$$I^2 = 2\pi\int_{\sqrt{800}}^{\infty} r\exp(-kr^2)\,dr = \pi\int_{800}^{\infty}\exp(-kr^2)\,dr^2$$

$$I^2 = \frac{-\pi}{k}\exp(-kr^2)\Big|_{800}^{\infty} = \frac{\pi}{k}\exp(-800k)$$

$$I = \sqrt{\frac{\pi}{k}}\exp(-400k)$$

Thus

$$\int\limits_{400}^{\infty} \sqrt{E}\exp(\frac{-3E}{2\varepsilon})dE = -2\frac{\partial}{\partial k}I = -2\frac{\partial}{\partial k}\sqrt{\frac{\pi}{k}}\exp(-400k)$$

$$\int\limits_{400}^{\infty} \sqrt{E}\exp(\frac{-3E}{2\varepsilon})dE = \frac{1}{k}\sqrt{\frac{\pi}{k}}\exp(-400k) + 800\sqrt{\frac{\pi}{k}}\exp(-400k)$$

ultimately yielding

$$\int\limits_{400}^{\infty} \sqrt{E}\exp(\frac{-3E}{2\varepsilon})dE = \sqrt{\frac{2\pi\varepsilon}{3}}\exp(-600/\varepsilon)\,[\frac{2\varepsilon}{3}+800] \qquad \textbf{A-9}$$

75

The evaluation of the integrals in equation A-2 therefore become

$$\langle \frac{V_i}{P} \rangle = 6 \times 10^7 \sqrt{\frac{27}{2\pi}} \, \varepsilon^{-3/2} \{ \frac{2\alpha\beta\varepsilon}{2\varepsilon+3\beta} [\frac{8(\beta\varepsilon)^2}{(2\varepsilon+3\beta)^2} + \frac{4\beta\varepsilon E_i}{2\varepsilon+3\beta} + E_i^2] \exp(\frac{-3E_i}{2\varepsilon})$$

$$- \frac{2\alpha\beta\varepsilon E_i}{2\varepsilon+3\beta} (\frac{2\beta\varepsilon}{2\varepsilon+3\beta} + E_i) \exp(\frac{-3E_i}{2\varepsilon})$$

$$+ 10^2 \sqrt{\frac{2\pi\varepsilon}{3}} \, \exp(\frac{-600}{\varepsilon}) (\frac{2\varepsilon}{3} + 800) \} \qquad \text{A-10}$$

Appendix B

Derivation of the Effective E-Field

for Short Electromagnetic Pulses

Consider the effective electromagnetic field for continuous wave phenomenon[6].

$$E_{eff} = \frac{E}{[2(1+\frac{\omega^2}{v_{eff}^2})]^{1/2}}$$ B-1

It is desired to obtain the effective electromagnetic field for a short electromagnetic pulse, which contains a spectrum of frequencies. For simplicity assume that the electromagnetic pulse is a sawtooth waveform as shown in Figure B-1.
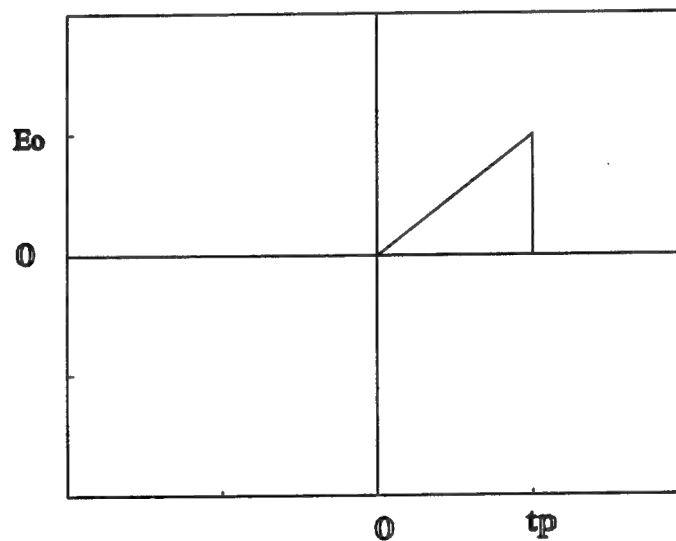
Figure B-1. E-field vs. Time

This waveform is described by

$$E(t) = E_o \frac{t}{t_p}$$
B-2

where:

E_o = Peak electric field

t = time

t_p = pulse duration

for

$$0 \le t \le t_p$$

and zero elsewhere. The Fourier series of this sawtooth waveform is

$$E(t) = \sum_{n=1}^{\infty} (-1)^{n+1} \frac{2E_o}{n\pi} \sin\left(\frac{n\pi t}{t_p}\right)$$
B-3

where $n\pi/t_p$ is the component frequency, and $(-1)^{n+1} 2E_o/n\pi$ is the E-field due to each frequency component. The effective E-field at each frequency component is obtained by substitution of the E-field due to each frequency component of equation B-3 into B-1. This operation yields,

$$E_{eff}\left(\omega = \frac{n\pi}{t_p}\right) = \frac{(-1)^{n+1}}{n\pi} \frac{2E_o}{\left[2\left(1 + \frac{n^2\pi^2}{t_p^2 v_{eff}^2}\right)\right]^{1/2}}$$
B-4

79

To obtain the total effective E-field it is necessary to sum over all frequencies.

$$E_{eff} = \sqrt{2} E_o \sum_{n-1}^{\infty} \frac{(-1)^{n+1}}{n\pi (1+\frac{n^2\pi^2}{t_p^2 v_{eff}^2})^{1/2}}$$ B-5

Recalling once more[20] that $v_{eff}=5.3 \times 10^9 P$ yields

$$E_{eff} = E_o \sum_{n-1}^{\infty} \frac{\sqrt{2} (-1)^{n+1}}{n\pi (1+\frac{n^2\pi^2}{2.809 \times 10^{19} t_p^2 P^2})^{1/2}}$$ B-6

The summation of the first 100 terms contained in equation B-6 is plotted in Figure B-2, on page 81, as a function of pulse length multiplied by pressure. The asymptotical value for the summation is approximately 0.310 for the region of interest of this investigation. Therefore, equation B-6 may be rewritten as

$$E_{eff} \approx 0.310 E_o$$ B-7

At higher pressures this value is achieved for shorter pulse lengths, while at lower pressures a longer pulse length is required. Figure B-2 indicates that: a large applied E-field can be scaled into an appropriately small effective E-field with the selection of an adequately short pulse, and as pressure decreases so does the effective E-field.

80
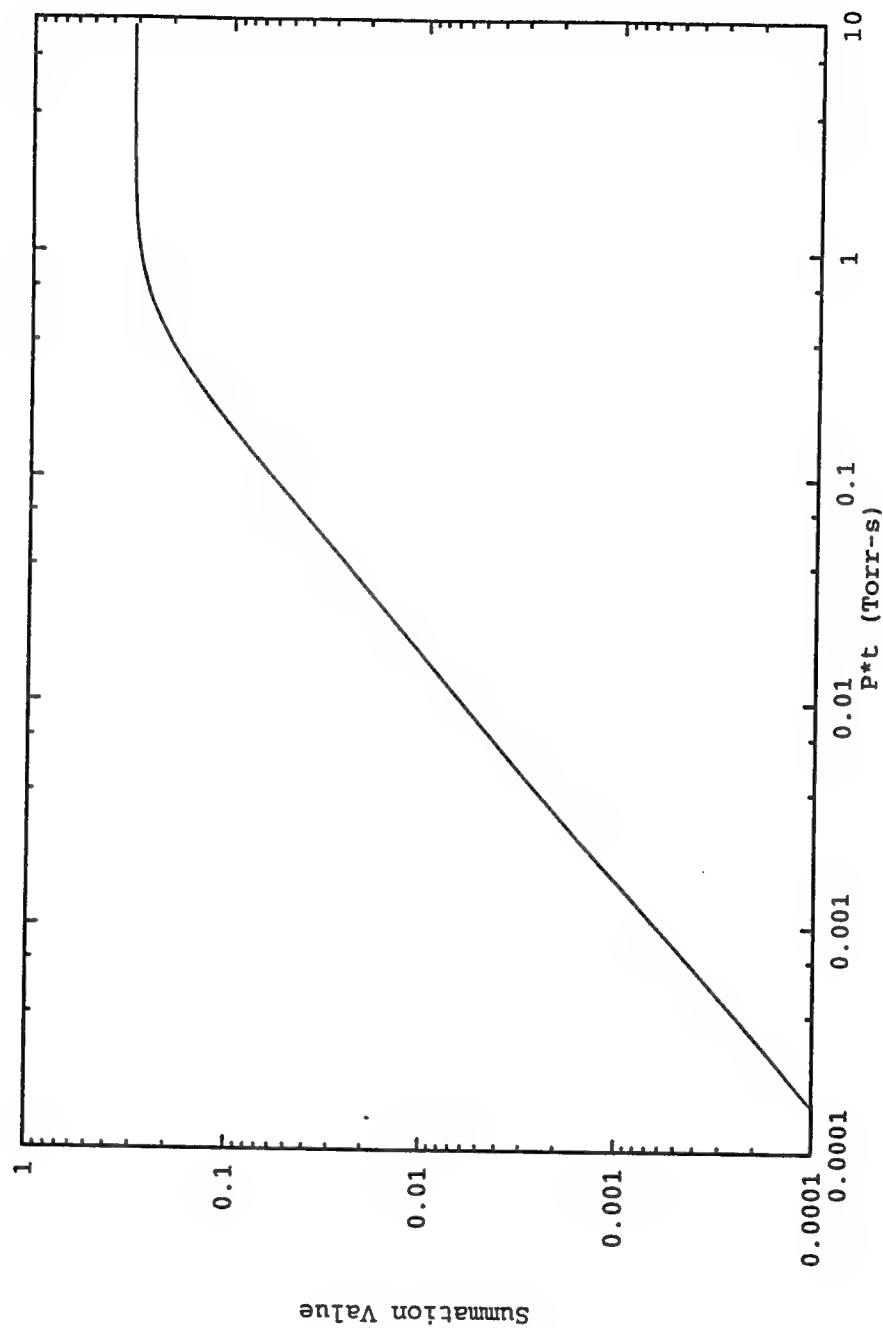
Figure B-2. Summation Value vs. Pulse Length

Appendix C

Relativistic Derivation of the

Paschen Curve

for Short Electromagnetic Pulses

Consider relativistic scattering by a central force, as shown in figure C-one below.

Figure C-One.   Scattering by a Central Force.

where: $b \equiv$ impact parameter

$d\Omega \equiv$ differential solid angle for a unit

radius sphere ($2\pi r\sin\theta d\theta$, with r=1)

$\Gamma_{in} \equiv$ incident particle flux

$\Gamma_{out} \equiv$ particle flux scattered into $d\Omega$ at θ

$d\sigma \equiv$ particle flux scattered into $d\Omega$ at θ, divided

by Γ_{in}

Following the method of Cherrington[34], the differential cross section can be defined as

$$\frac{d\sigma}{d\Omega} = \frac{particle\text{-}flux\text{-}into\text{-}d\Omega/d\Omega}{\Gamma_{in}}\Big|_b = \frac{\Gamma_{out}}{\Gamma_{in}}\Big|_\theta$$

Conservation of particles requires that

$$\Gamma_{in}(2\pi b \, db) - \Gamma_{out}(2\pi \sin\theta \, d\theta)$$

Therefore via substitution,

$$\frac{d\sigma}{d\Omega} - \frac{\Gamma_{out}}{\Gamma_{in}}\Big|_\theta - \frac{2\pi b \, db}{2\pi \sin\theta \, d\theta} - \frac{b}{\sin\theta}\Big|\frac{db}{d\theta}\Big| \qquad\qquad \textbf{C-1}$$

The relationship between b and θ is

$$\frac{\pi-\theta}{2} - \int_0^{u_{max}} \frac{du}{[\frac{1}{b^2}(1-\frac{V}{E})-u^2]^{1/2}} \qquad\qquad \textbf{C-2}$$

where: $u = 1/R$

   E = kinetic energy

   V = potential energy

The electric field for a relativistic particle is

$$E - \frac{Q}{4\pi\varepsilon_o R^2 \gamma^2 (1-\beta^2\sin^2\phi)^{3/2}}$$

where: Q = electron charge (1.602×10^{-19} Coul.)

   ε_o = electric permittivity

   β = v/c

   $\gamma = (1-\beta^2)^{-1/2}$.

84

The potential energy for a repulsive interaction then becomes

$$V = q\varphi(R,\phi) = \frac{Q^2}{4\pi\varepsilon_o R\gamma^2 (1-\beta^2\sin^2\phi)^{3/2}} \qquad \text{C-3}$$

Noting from figure C-1 that $\sin\Phi = b/R$, equation C-3 may be rewritten as

$$V = \frac{Q^2}{4\pi\varepsilon_o R\gamma^2 [1-(\frac{\beta b}{R})^2]^{3/2}}$$

For compactness of notation the quantity k is now defined as

$$k = \frac{Q^2}{4\pi\varepsilon_o}$$

so that

$$V = \frac{k}{\gamma^2 R[1-(\frac{\beta b}{R})^2]^{3/2}} = \frac{uk}{\gamma^2 [1-(\beta bu)^2]^{3/2}}$$

Equation C-2 may now be written as

$$\frac{\pi-\theta}{2} = \int_0^{u_{max}} \frac{du}{\{\frac{1}{b^2}[1-\frac{uk(v)}{\gamma^2 E(1-(\beta bu)^2)^{3/2}}]-u^2\}^{1/2}} \qquad \text{C-4}$$

85

To evaluate the integral in equation C-4 it is necessary to determine u_{max}. This is accomplished by beginning with the law of conservation of momentum.

$$\gamma m_o v b = \gamma_{R\phi} m_o R (R\dot\phi) = \gamma_{R\phi} m_o R^2 \dot\phi$$

which may be rewritten as

$$\frac{\gamma v b}{R^2} = \frac{\dot\phi}{\sqrt{1-(\frac{R\dot\phi}{c})^2}}$$

Solving for the time derivative of ϕ yields

$$\dot\phi = \frac{\gamma v b}{R^2\sqrt{1+(\frac{\gamma\beta b}{R})^2}} \qquad\qquad \text{C-5}$$

which reduces to the classical answer when v<<c, such that $\beta\approx0$ and $\gamma\approx1$. The law of conservation of energy requires that

$$(\gamma-1) m_o c^2 = (\gamma_R-1) m_o c^2 + (\gamma_{R\phi}-1) m_o c^2 + \frac{k}{\gamma^2 R(1-\frac{\beta^2 b^2}{R^2})^{3/2}} \qquad \text{C-6}$$

where

$$\gamma_R = \frac{1}{\sqrt{1-(\frac{\dot R}{c})^2}}$$

86

and

$$\gamma_{R\phi} = \frac{1}{\sqrt{1 - (\frac{R\dot\phi}{c})^2}}$$

The quantity of interest, u_{max}, is evaluated at that point in space at which the radial velocity is zero.

$$u_{max} = \frac{1}{R}\Big|_{\dot R = 0}$$

This drives the first term on the right hand side of equation C-6 to zero. Thus equation C-6 may be rewritten as

$$(\gamma - 1) m_o c^2 = (\gamma_{R\phi} - 1) m_o c^2 + \frac{k}{\gamma^2 R (1 - \frac{\beta^2 b^2}{R^2})^{3/2}}$$

$$\gamma m_o c^2 = \gamma_{R\phi} m_o c^2 + \frac{k}{\gamma^2 R (1 - \frac{\beta^2 b^2}{R^2})^{3/2}}$$

Combining C-5 and C-7 into the above equation yields

$$\gamma m_o c^2 = m_o c^2 \sqrt{1 + (\frac{\gamma \beta b}{R})^2} + \frac{k}{\gamma^2 R (1 - \frac{\beta^2 b^2}{R^2})^{3/2}}$$

It is noted that the classical solution for u_{max} goes to 1/b as velocities increase. This implies that a relativistic solution should yield approximately the same answer. To simplify the solution of equation C-8, the second term on the right hand side is approximated for $R \approx b$ and $\beta \approx 1$ as

$$\frac{k}{\gamma^2 R (1 - \frac{\beta^2 b^2}{R^2})^{3/2}} \sim \frac{k}{\gamma^2 R (1 - \beta^2)^{3/2}} = \frac{k\gamma^3}{\gamma^2 R} = \frac{\gamma k}{R} \qquad \text{C-9}$$

Therefore equation C-8 becomes

$$\gamma m_o c^2 = m_o c^2 \sqrt{1 + (\frac{\gamma \beta b}{R})^2} + \frac{\gamma k}{R}$$

Solving for 1/R yields

$$u_{max} = \frac{1}{R}\Big|_{R=0} = \frac{\frac{2\gamma^2 k}{m_o c^2} \pm \sqrt{(\frac{2\gamma^2 k}{m_o c^2})^2 - 4[(\frac{\gamma k}{m_o c^2})^2 - (\gamma \beta b)^2](\gamma^2 - 1)}}{2[(\frac{\gamma k}{m_o c^2})^2 - (\gamma \beta b)^2]}$$

$$= \frac{\frac{k}{m_o c^2} \pm \sqrt{(\frac{k}{m_o c^2})^2 - \frac{1}{\gamma^2}(\gamma^2 - 1)[(\frac{k}{m_o c^2})^2 - (\beta b)^2]}}{[(\frac{k}{m_o c^2})^2 - (\beta b)^2]} \qquad \text{C-10}$$

Noting that

$$\frac{1}{\gamma^2}(\gamma^2-1)=\beta^2$$

Equation C-10 becomes

$$u_{max}=\frac{\dfrac{k}{m_oc^2}\pm\sqrt{(\dfrac{k}{m_oc^2})^2-\beta^2[(\dfrac{k}{m_oc^2})^2-(\beta b)^2]}}{[(\dfrac{k}{m_oc^2})^2-(\beta b)^2]}$$

which can be rewritten as

$$u_{max}=\frac{\dfrac{k}{m_oc^2\beta^2b^2}\pm\sqrt{(\dfrac{k}{\gamma m_oc^2\beta^2b^2})^2+\dfrac{1}{b^2}}}{[(\dfrac{k}{m_oc^2\beta b})^2-1]}$$

The denominator is functionally equal to minus one. Thus

$$u_{max}\approx-\frac{k}{m_oc^2\beta^2b^2}+\sqrt{(\frac{k}{\gamma m_oc^2\beta^2b^2})^2+\frac{1}{b^2}}\qquad\textbf{C-11}$$

which yields the classical solution for v<<c, and yields $u_{max}=1/b$ for v≈c.

89

It is also possible to obtain the critical impact parameter, b_{crit}, and hence calculate the inelastic collisional cross section. b_{crit} is defined to be the solution for b when R_{min} is negative or complex. Recalling the equation prior to C-11

$$R_{min} = \frac{1}{u_{max}} = \frac{[(\frac{k}{m_oc^2\beta b})^2]-1}{\frac{k}{m_oc^2\beta^2b^2} \pm \sqrt{(\frac{k}{\gamma m_oc^2\beta^2b^2})^2 + \frac{1}{b^2}}} \qquad \text{C-12}$$

which yields a b_{crit} of

$$b_{crit} < \frac{k}{m_oc^2\beta^2}\beta = \frac{k}{\beta m_oc^2} \qquad \text{C-13}$$

Thus the inelastic cross section becomes

$$\sigma(\beta)_{inelastic} = \pi b_{crit}^2 = \frac{\pi k^2}{(m_oc^2)^2\beta^2} \qquad \text{C-14}$$

Rewriting in terms of energy

$$\sigma(E)_{inelastic} = \pi b_{crit}^2 = \frac{\pi k^2}{(m_oc^2)^2[1-\frac{1}{1+\frac{E}{m_oc^2}}]} \qquad \text{C-15}$$

90

u_{max} having been obtained, the integral C-4 may now be evaluated.

$$\frac{\pi-\theta}{2} = \int_0^{u_{max}} \frac{du}{\{\frac{1}{b^2}[1-\frac{uk}{\gamma^2 E(1-(\beta bu)^2)^{3/2}}]-u^2\}^{1/2}}$$

Recall from equation C-9

$$\frac{k}{\gamma^2(1-\beta^2 b^2 u^2)^{3/2}} \approx \frac{k}{\gamma^2(1-\beta^2)^{3/2}} = \frac{k\gamma^3}{\gamma^2} = \gamma k$$

therefore

$$\frac{\pi-\theta}{2} = \int_0^{u_{max}} \frac{du}{\{\frac{1}{b^2} - \frac{\gamma k}{Eb^2}u - u^2\}^{1/2}} \tag{C-16}$$

This equation is merely the classical equation for a repulsive coulomb interaction with the second term of the denominator modified by the relativistic γ. Immediately utilizing the classical results, and replacing the classical "k" with the relativistic "γk" yields the solution

$$\frac{\pi-\theta}{2} = -\sin^{-1}\frac{[-2u-\frac{\gamma k}{Eb^2}]}{[\frac{4}{b^2}+(\frac{\gamma k}{Eb^2})^2]^{1/2}}\Big|_0^{u_{max}} \tag{C-17}$$

91

At relativistic velocities $u_{max} \rightarrow 1/b$. Therefore

$$\frac{\theta-\pi}{2} = \sin^{-1}\frac{-[\frac{2}{b}+\frac{\gamma k}{Eb^2}]}{[\frac{4}{b^2}+(\frac{\gamma k}{Eb^2})^2]^{1/2}} - \sin^{-1}\frac{-(\frac{\gamma k}{Eb^2})}{[\frac{4}{b^2}+(\frac{\gamma k}{Eb^2})^2]^{1/2}} \qquad \text{C-18}$$

The term contained by the first arcsin on the right hand side of C-18 goes to -1 as $v \rightarrow c$. This allows C-18 to be reduced to

$$\frac{\theta}{2} = \sin^{-1}\frac{(\frac{\gamma k}{Eb^2})}{[\frac{4}{b^2}+(\frac{\gamma k}{Eb^2})^2]^{1/2}}$$

which can be written more compactly as

$$\theta = 2\tan^{-1}\frac{\gamma k}{2Eb} \qquad \text{C-19}$$

Equation C-19 reduces to the classically obtained result when $\gamma \rightarrow 1$. Solving for b yields,

$$b = \frac{\gamma k}{2E}\cot(\frac{\theta}{2}) \qquad \text{C-20}$$

Recalling C-1

$$\frac{d\sigma}{d\Omega} = \frac{b}{\sin\theta}|\frac{db}{d\theta}| = \frac{1}{4}(\frac{\gamma k}{2E})^2\frac{1}{\sin^4(\frac{\theta}{2})}$$

92

The integral for the collisional cross section then becomes

$$\sigma_c(\theta) = \int_{\theta_{min}}^{\pi} \frac{d\sigma}{d\Omega} d\Omega = \frac{1}{4} \left(\frac{\gamma k}{2E}\right)^2 \int_{\theta_{min}}^{\pi} \frac{d\Omega}{\sin^4\left(\frac{\theta}{2}\right)} \qquad \text{C-21}$$

which yields

$$\sigma_c(\theta) = \pi \left(\frac{\gamma k}{2E}\right)^2 \cot^2\left(\frac{\theta_{min}}{2}\right) \qquad \text{C-22}$$

where θ_{min} is θ evaluated at b set equal to the species debye length λ_d.

The solutions for σ_m and σ_E are also desired, where σ_m is the forward momentum transfer cross section, and σ_E is the energy cross section. These parameters are defined as followed.

$$\sigma_m(\theta) = \int_{\theta_{min}}^{\pi} \frac{d\sigma}{d\Omega} [1 - \cos(\theta)] 2\pi \sin(\theta) d\theta$$

$$\sigma_E(\theta) = \int_{\theta_{min}}^{\pi} \frac{d\sigma}{d\Omega} [1 - \cos(\theta)] \left(\frac{2m_o}{M}\right) 2\pi \sin(\theta) d\theta$$

93

The classical solutions immediately show that

$$\sigma_m(E) = 16\pi\left(\frac{\gamma k}{4E}\right)^2 \ln\left(\frac{2E\lambda_d}{\gamma k}\right) \qquad \text{C-23}$$

$$\sigma_E(E) = \frac{2m_o}{M}\sigma_m(E) \qquad \text{C-24}$$

Thus, the solutions for all three collision cross sections contain the species debye length. The species debye length is itself subject to relativistic effects. The debye length is defined to be

$$\lambda_d = \left(\frac{\varepsilon_o k_B T_e}{n_o Q^2}\right)^{1/2} = \sqrt{\frac{\varepsilon_o}{n_o Q}}\left(\frac{k_B T_e}{Q}\right)^{1/2}$$

where: n_o = electron density in particles per cubic meter

k_B = Boltzmann's constant

T_e = electron temperature

$k_B T_e$ = electron kinetic energy in eV

The relativistic kinetic energy is

$$E = (\gamma - 1)m_o c^2$$

94

Thus,

$$\lambda_d = \sqrt{\frac{\varepsilon_o}{n_o Q}} \sqrt{\frac{E}{Q}}$$

At breakdown the ratio of the final electron density to the initial electron density has been determined[23] to be 10^8. At approximately standard temperature and pressure the free electron density has been estimated[36] to be between 0.1 to 10 electrons per cubic meter. This investigation will assume a free electron density of one electron per cubic meter. Utilizing the ideal gas law, $PV = n_{mole} R_o T$ where: P is pressure in atmospheres, V is volume in liters, n_{mole} is the number of moles, R_o is the gas law constant of 0.08205 atm*l/mole/°K, and T is the temperature in degrees Kelvin, the initial electron density n_o may be estimated as

$$n_o = 23.8x10^8 \frac{n_{mole}}{V} = 23.8x10^8 \frac{P}{R_o T}$$

where the factor of $23.8x10^8$ in the numerator is in units of electrons*liters per mole*ms³. Substituting in for n_o

$$\lambda_d = \sqrt{\frac{\varepsilon_o R_o T}{23.8x10^8 PQ}} \sqrt{\frac{E}{Q}} \qquad\qquad \text{C-25}$$

95

Substituting equation C-25 into equation C-19 yields a θ_{min} of

$$\theta_{min} = 2\tan^{-1}\frac{\gamma k}{2E}\sqrt{\frac{23.8 \times 10^8 Q^2 P}{\varepsilon_o R_o TE}}$$

Therefore equation C-22 evaluates as

$$\sigma_c = \frac{\pi \varepsilon_o R_o T}{23.8 \times 10^8 Q^2 P}E \qquad\qquad \text{C-26}$$

which, except for the energy term, is independent of γ. Equations C-23 and C-24 become

$$\sigma_m(E) = 16\pi\left(\frac{\gamma k}{4E}\right)^2 \ln\left(\frac{2E}{\gamma k}\sqrt{\frac{\varepsilon_o R_o TE}{23.8 \times 10^8 Q^2 P}}\right) \qquad\qquad \text{C-27}$$

$$\sigma_E(E) = 16\pi\frac{2m_o}{M}\left(\frac{\gamma k}{4E}\right)^2 \ln\left(\frac{2E}{\gamma k}\sqrt{\frac{\varepsilon_o R_o TE}{23.8 \times 10^8 Q^2 P}}\right) \qquad\qquad \text{C-28}$$

Noting that $\gamma = 1 + E/m_o c^2$, C-27 maybe rewritten as

$$\sigma_m(E) = \pi\left[\frac{k}{E}\left(1 + \frac{E}{m_o c^2}\right)\right]^2 \ln\left(\frac{2}{k}\sqrt{\frac{\varepsilon_o R_o TE}{23.8 \times 10^8 PQ^2}}\frac{E}{1 + \frac{E}{m_o c^2}}\right) \qquad \text{C-29}$$

while equation C-28 is still

$$\sigma_E(E) = \frac{2m_o}{M}\sigma_m(E) \qquad\qquad \text{C-30}$$

Therefore, with the use of equation 7 of the main text and a standard text reference[34],

$$v_i = N_{N_2}\int_{E_1}^{\infty}\sigma(E)_{inelastic}\sqrt{\frac{2E}{m_e}}\,\frac{2}{\sqrt{\pi}}\sqrt{\frac{E}{\frac{2}{3}\varepsilon}}\exp\left(\frac{-3E}{2\varepsilon}\right)\frac{dE}{\frac{2}{3}\varepsilon} \qquad \text{C-31}$$

$$v_c = N_{N_2}\int_{E_1}^{\infty}\sigma_c(E)\sqrt{\frac{2E}{m_e}}\,\frac{2}{\sqrt{\pi}}\sqrt{\frac{E}{\frac{2}{3}\varepsilon}}\exp\left(\frac{-3E}{2\varepsilon}\right)\frac{dE}{\frac{2}{3}\varepsilon} \qquad \text{C-32}$$

$$v_m = N_{N_2}\int_{E_1}^{\infty}\sigma_m(E)\sqrt{\frac{2E}{m_e}}\,\frac{2}{\sqrt{\pi}}\sqrt{\frac{E}{\frac{2}{3}\varepsilon}}\exp\left(\frac{-3E}{2\varepsilon}\right)\frac{dE}{\frac{2}{3}\varepsilon} \qquad \text{C-33}$$

where C-31, C-32 and C-33 all have units of s^{-1}. Substitution of C-15, C-26, and C-29 into C-31, C-32 and C-33 respectively yields

97

$$\nu_i = 6.02 \times 10^{26} \frac{P}{R_o T} \sqrt{\frac{27\pi}{m_e}} \left(\frac{k}{m_e c^2}\right)^2 \varepsilon^{\frac{-3}{2}} \int_{E_1}^{\infty} \frac{E \exp\left(\frac{-3E}{2\varepsilon}\right)}{[1 - \frac{1}{1 + \frac{E}{m_e c^2}}]} dE \qquad \text{C-34}$$

$$\nu_c = \frac{6.02 \times 10^{26}}{23.8 \times 10^8} \sqrt{\frac{27\pi}{m_e}} \left(\frac{\varepsilon_o}{Q^2}\right) \varepsilon^{-\frac{3}{2}} \int_{E_1}^{\infty} E^2 \exp\left(\frac{-3E}{2\varepsilon}\right) dE \qquad \text{C-35}$$

$$\nu_m = 6.02 \times 10^{26} \sqrt{\frac{27\pi}{m_e}} \frac{k^2 P}{R_o T} \varepsilon^{-\frac{3}{2}} \{ \qquad \text{C-36}$$

$$\int_{E_1}^{\infty} \frac{1}{E} \left(1 + \frac{E}{m_o c^2}\right)^2 \ln\left(\frac{2}{k} \sqrt{\frac{\varepsilon_o R_o T}{23.8 \times 10^8 P Q^2}} \frac{E^{\frac{3}{2}}}{1 + \frac{E}{m_o c^2}}\right) \exp\left(\frac{-3E}{2\varepsilon}\right) dE \}$$

Evaluating integral C-34 requires numerical integration. Dividing the integral by pressure in Torr, and equating with equation 5 of the main text yields

$$\frac{18.4}{P\tau_p} = \frac{7.92 \times 10^{23}}{R_o T} \sqrt{\frac{27\pi}{m_e}} \left(\frac{k}{m_e c^2}\right)^2 \varepsilon^{\frac{-3}{2}} \int_{E_1}^{\infty} \frac{E \exp\left(\frac{-3E}{2\varepsilon}\right)}{[1 - \frac{1}{1 + \frac{E}{m_e c^2}}]} dE \qquad \text{C-37}$$

Evaluating integral C-35 yields.

$$\nu_c = 2.53 \times 10^{17} \sqrt{\frac{12\pi}{m_e}} \left(\frac{\varepsilon_o}{Q^2}\right) \varepsilon^{-\frac{1}{2}} \exp\left(\frac{-3E_i}{2\varepsilon}\right) \left[\left(\frac{2\varepsilon}{3}\right)^2 + \right.$$

$$\left. 2E_i \left(\frac{2\varepsilon}{3}\right) + E_i^2\right] \qquad \qquad \text{C-38}$$

Integral C-36 requires numerical integration. From equation 17 of the main text it is recalled that

$$\varepsilon = \frac{Q^2 E_{eff}^2}{m_e \delta_{eff} \nu_{eff}^2} \qquad \qquad \text{C-39}$$

It is desired to obtain the relativistic effective electromagnetic field for a short electromagnetic pulse, which contains a spectrum of frequencies. Let the applied pulse shape be that selected in appendix B and begin by recalling equation B-5 which is still correct in the relativistic regimen.

$$E_{eff} = \sqrt{2} E_o \sum_{n-1}^{\infty} \frac{(-1)^{n+1}}{n\pi \left(1 + \frac{n^2\pi^2}{t_p^2 \nu_{eff}^2}\right)^{1/2}} \qquad \qquad \text{C-40}$$

It has been shown[23] to be inappropriate to assume that $\nu_{eff} = 5.3 \times 10^9 P$ with the ratio of the applied electric field to

99

pressure is in excess of 50 V/cm/Torr. Roussel-Dupré et. al.[23] has noted that for intense electric fields, which produce relativistic motion in electrons, the effective collision frequency is

$$v_{eff} = R_m + R_c \qquad \text{C-41}$$

where $R_m = 10^8 n_o v_m / V_{arc}$, $R_c = 10^8 n_o v_c / V_{arc}$, and V_{arc} is the volume of the arc.

Equations C-36 through C-41 constitute a set of existential equations. Since the experimental parameters of E_o, and P are typically known, the following strategy for the estimation of the breakdown curve was adopted. v_{eff} was first set equal to the classical value of $5.3 \times 10^9 P$, t_p was set equal to 1×10^{-5} s, and E_o was set equal to 200 V/cm. These values were then used to estimate E_{eff} based on equation C-40. From this value for E_{eff}, an estimate of ε was obtain in accordance with equation C-39. Utilizing this estimate of ε, an estimate of v_i and hence t_p was obtained via equation C-37. If the estimate of the pulse length differed from the previous estimate of the pulse length by greater than one percent, then a new estimate of E_{eff} was obtained and the process was iterated. If the value for the pulse length had converged, then estimates for v_c and v_m were obtained via equations C-36 and C-38. A new estimate for v_{eff} was then calculated via equation C-41. If

100

the new estimate of v_{eff} differed from the previous estimate by greater than one percent, then a new estimate of E_{eff} was obtained and the entire process was iterated until convergence to a final value was observed.

The results of this computation are shown in figure C-2, a plot of E_o/P versus $P\tau_p$. The ordinate represents E_o/P while the abscissa represents $P\tau_p$. The solid line is the theoretical curve of Graham and Roussel-Dupré[23]. The long dashed line is the theoretical curve as derived in the classical theory section of the main body. The short dashed line is the theoretical curve produced by the process described in this section.

Note that all three theories produce a reversal in the paschen curve. In the classically derived theory the reversal transitions into a vertical barrier. In the relativistic theory of Graham and Roussel-Dupré the reversal transitions through yet another reversal to reestablish the Paschen curve at a higher value of E_o/P. The relativistic theory developed in this section produces a reversal which continues into the upper right hand quadrant of the plot, which is attributed to the one dimensional nature of the theory.
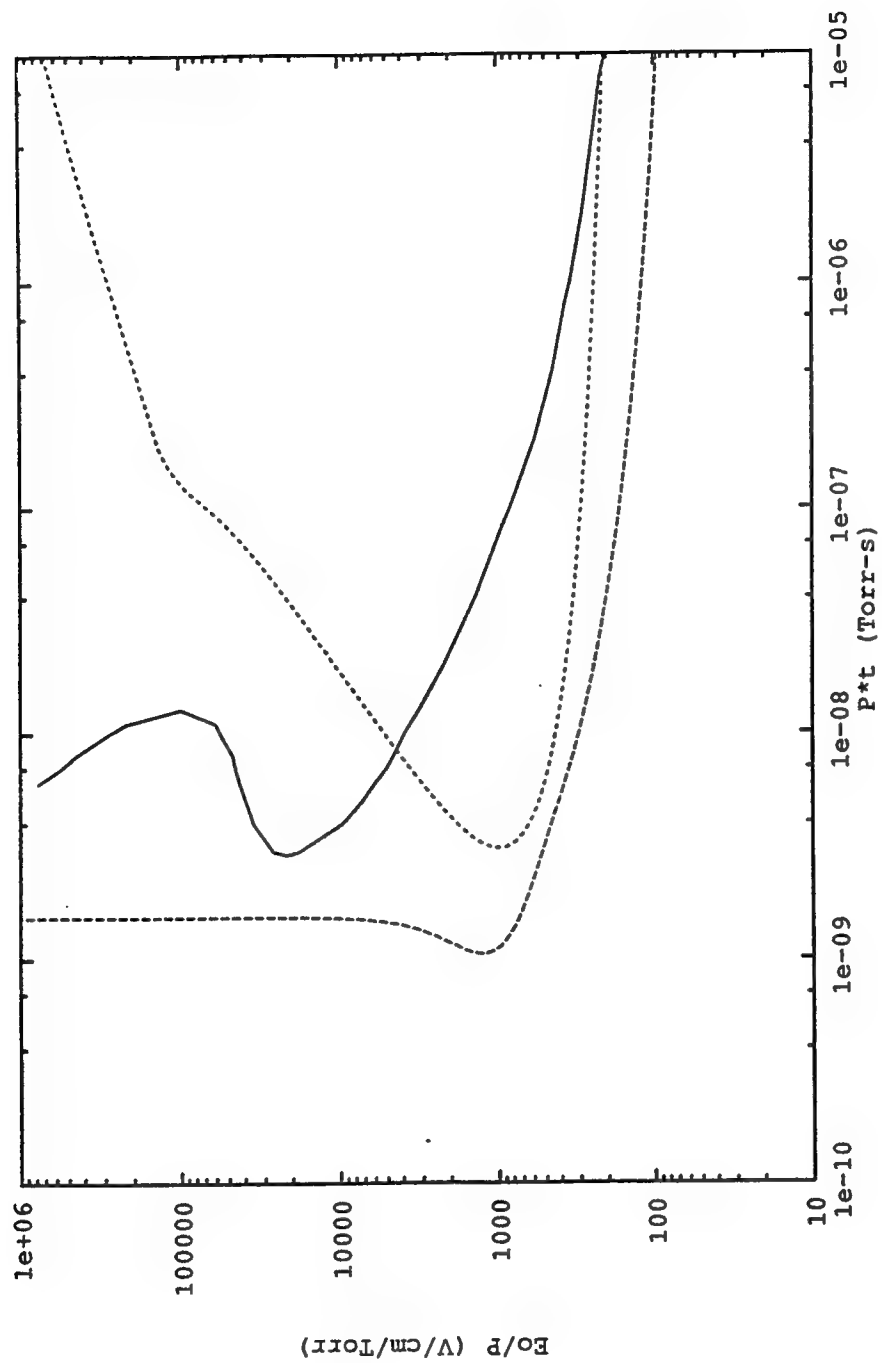
Figure C-2. Comparison of
Theoretical Paschen Curves

102

REFERENCES

1.) Vaulin V.A. and Slinko V.N., <u>A Nitrogen Laser Excited By Microwave Pulses</u>, Quantum Electronics, B.15, N 1, pp 61-62, 1988.

2.) Slinko V.N., Sulakshin A.S., and Sulakshin S.S., <u>Effective Stimulated Emission From A Microwave-Pumped XeCl Laser</u>, Quantum Electronics, B.15, N 2, pp 292-294, 1988.

3.) Vaulin V.A., Slinko V.N., and Sulakshin S.S., <u>A KrF Laser Excited By A High-Power Nanosecond Microwave Pulse</u>, Quantum Electronics, B.15, N 11, pp 3331-3333, 1988.

4.) Ali A.W., Coffey T., <u>Naval Research Laboratory Memorandum No. 4320</u>, 1980 (unpublished).

5.) Sullivan C.A., Destler W.W., Rodgers J., and Segalov Z., <u>Short-Pulse High-Power Microwave Propagation in the Atmosphere</u>, Journal of Applied Physics, Vol.63, No. 11, 1 June 1988.

6.) MacDonald A.D., <u>Microwave Breakdown in Gases</u>, Wiley, New York, 1966.

7.) Felsenthal P., Proud J.M., <u>Nanosecond Pulse Breakdown in Gases</u>, Physical Review, pp 1796-1804, Sept 1965.

8.) Tetenbaum S.J., MacDonald A.D., and Bandel H.W., <u>Pulsed Microwave Breakdown of Air From 1 Torr to 1000 Torr</u>, Journal of Applied Physics, Vol. 42, pg 5871, 1971.

9.) Divergilio W.F., Thomson J.J., <u>High Power Microwave Breakdown Experimental Design Study</u>, AD-A176 941, Feb. 1982.

10.) Bollen W.M. et. al., <u>High Power Microwave Energy Coupling to Nitrogen During Breakdown</u>, Journal of Applied Physics, Vol. 54, No. 1, Jan. 1983.

11.) Gold S.H., Black W.M., Granatstein V.L., and Kinkead A.K., <u>Breakdown of the Atmosphere by Emission From a Millimeter-wave Free-Electron Maser</u>, Applied Physics Letters, Vol. 43, No. 10, 15 Nov. 1983.

12.) Didenko A.N., Novikov S.A., Razin S.V., Chumerin P. Yu, and Yushkov Yu G., <u>Breakdown of a Waveguide Channel During the Propagation of High-Power Nanosecond Microwave Pulses</u>, Soviet Journal of Communications Technology and Electronics, Vol. 30, No. 7, July 1985.

13.) Didenko A.N., Petrov V.M., Slinko V.N., Sulakshin S.S., and Yushkov Yu G., <u>Supercooled Plasma in High Power Microwave Discharges</u>, Soviet Physics - Doklady, Vol. 32, No. 1, Jan 1987.

14.) Slinko V.N., Sulakshin S.S., and Sulakshina L.V., <u>On Producing an Extended Microwave Discharge at High Pressure</u>, Soviet Physics Technical Physics, Vol. 33, No. 3, March 1988.

15.) Didenko A.N., Prokhorov A.M., Slinko V.N., Sulakshin A.S., and Sulakshin S.S., <u>Pumping of Ultraviolet Gas Lasers By a High-Power Pulsed Radiation From a Relativistic Microwave Generator</u>, Soviet Physics - Doklady, Vol. 33, No. 6, June 1988.

16.)   Slinko V.N., Sulakshina L.V., and Sulakshin S.S., Total
Absorption of a High Power Microwave Pulse in a Collisional
Plasma, Soviet Technical Physics Letters, Vol. 14, No. 10,
Oct. 1988.

17.)   Vaulin V.A., Slinko V.N., and Sulakshin S.S., Air
Ultraviolet Laser Excited by High Power Microwave Pulses,
Soviet Journal of Quantum Electronics, Vol. 18, No. 11, Nov.
1988.

18.)   Baranov S.V., Vaulin V.A., Lomaev M.I., Slinko V.N.,
Sulakshin S.S., and Tarasenko V.F., Use of High Power
Microwave Pumping for Plasma Lasers, Soviet Journal of Quantum
Electronics, Vol. 19, No. 3, March 1989.

19.)   Destler W.W., Segalov Z., and Rodgers J., Shielded-
Source Short Pulse Microwave Propagation Experiments, Journal
of Applied Physics, Vol. 66, No. 3, Aug. 1989.

20.)   Vaulin V.A., Romanovich V.V., Slinko V.N., Sulakshina
L.V., Sulakshin S.S., Production of Large Volume Microwave
Discharges in High Pressure Gases, Soviet Physics Technical
Physics, Vol. 35, No. 2, Feb. 1990.

21.)   Zakharenko O.A., Kuznetsov A.A., Slinko V.N., and
Sulakshin S.S., Experimental Investigations of Vacuum
Ultraviolet Emission From Kr and Xe Rare Gases in a High Power
High-Pressure Pulsed Microwave Discharge, Soviet Journal of
Quantum Electronics, Vol. 20, No. 7, July 1990.

22.) Vaulin V.A., Slinko V.N., and Sulakshin S.S., <u>Excimer XeCl Laser Excited by Microsecond Megawatt Microwave Pulses From a Commercial 3.07 GHz. Microwave Oscillator</u>, Soviet Journal Quantum Electronics, Vol. 20, No. 12, Dec. 1990.

23.) Graham G, and Roussel-Dupré R.A., <u>Air Breakdown in the Relativistic Limit</u>, Technical Documentary Report No. CONF-8905184--1, Los Alamos National Laboratory, Dec. 1989.

24.) Scharfman W.E., Taylor W.C., and Morita T., <u>Breakdown Limitations on the Transmission of Microwave Power Through the Atmosphere</u>, IEEE Transactions on Antennas and Propagation, AP-12, November 1964.

25.) Gould L., and Roberts L.W., <u>Breakdown at Microwave Frequencies</u>, Journal of Applied Physics, Vol. 27, pg 1162, 1956.

26.) Lupan Y.A., <u>Refined Theory for an RF Discharge in Air</u>, Soviet Physics Technical Physics, Vol. 21, No. 11, Nov. 1976.

27.) McDaniel E.W., <u>Collision Phenomena in Ionized Gases</u>, pg 198, Wiley, New York, 1964.

28.) Jackson J.D., <u>Classical Electrodynamics</u>, sec 11.10, 2nd Ed., Wiley, New York, 1975.

29.) Balanis C.A., <u>Antenna Theory</u>, pg 105, Wiley, New York, 1982.

30.) Weast, <u>Handbook of Chemistry and Physics</u>, 60th Ed., pp E-286 to E-287, Chemical Rubber Company Press, Florida, 1980.

31.) Armstrong W.T., Roussel-Dupré R.A., Karl R.R., Buchwald M.I., Graham G., Spectral Signatures From Short-Pulse Microwave Air Breakdown, Technical Documentary Report No. LA-UR-87-137, Los Alamos National Laboratory.

32.) Gahl J., Personal conversations with John Gahl.

33.) Englert T.J., Mullins B.W., Personal conversations with Thad Englert and Bill Mullins, Phillips Laboratory, Kirtland A.F.B., N.M. 26 March 1993.

34.) Cherrington B.E., Gaseous Electronics and Gas Lasers, 1st Ed., pp 50 to 51, Pergamon Press, New York, 1979.

35.) Roussel-Dupré R., Personal conversation with Robert Roussel-Dupré, Los Alamos National Laboratory, Los Alamos, N.M. 16 July 1992.

36.) Orear J., Rosenfeld A.H., and Schluter R.A., Nuclear Physics, University of Chicago Press, Chicago, 1949, (compilation of notes from lectures by Enrico Fermi).